

**PARTICLE IMAGE VELOCIMETRY APPLIED TO
MIXED CONVECTION IN A RECTANGULAR ENCLOSURE**

**PARTICLE IMAGE VELOCIMETRY APPLIED TO
MIXED CONVECTION IN A RECTANGULAR ENCLOSURE**

By

Karen M. Barrick, B.Eng.

A Thesis
Submitted to the School of Graduate Studies
in Partial Fulfilment of the Requirements
for the Degree
Master of Engineering

McMaster University

© Copyright by Karen M. Barrick, February 1995

MASTER OF ENGINEERING (1995)
(Mechanical)

McMASTER UNIVERSITY
Hamilton, Ontario

TITLE: Particle Image Velocimetry Applied to Mixed Convection in
a Rectangular Enclosure

AUTHOR: Karen Barrick, B.Eng. (McMaster University)

SUPERVISORS: Dr. M. Shoukri
Dr. P. Wood

NUMBER OF PAGES: (xi), 94

ABSTRACT

An investigation of mixed convection in a rectangular enclosure is presented in which the velocity fields in the enclosure are determined using Particle Image Velocimetry (PIV). Basically, this technique records optical images of flow tracers within a flow field, and determines the velocity field by measuring the displacement of the flow tracers during short time intervals. The components which comprise the PIV system and its operation are described in detail to familiarize the reader with this relatively new technique. The main objective of this investigation is to determine the accuracy and applicability of the PIV technique as a velocity measurement tool. This is accomplished by comparing present experimental velocity results to those obtained by Nurnberg [2] using Laser Doppler Anemometry (LDA). LDA has been proven to be an accurate velocity measurement tool and provides data for evaluating PIV results. A second objective of this research is to use the PIV results to verify a numerical code written by Nurnberg [2] which predicts the velocity fields in the rectangular enclosure. However, the comparison of experimental results of the two measurement techniques revealed that the PIV results were too inaccurate to perform this function. The large amount of error present in this PIV system prompted the recommendation of an improved, more accurate system. Although this improved system is very expensive - approximately \$40,000 - it will provide velocity measurements with an accuracy close to that of LDA, at half the cost of an LDA system and with far less time for data acquisition and analysis.

ACKNOWLEDGEMENTS

The author would like to express her appreciation to the following people for their assistance in the completion of this thesis:

- Dr. M. Shoukri and Dr. P. Wood for their guidance and financial support throughout the course of my research
- Dr. G. Nurnberg and Dr. D. Johnson for their advice and assistance
- The Mechanical Engineering department technicians, especially Mr. Ron Lodewyks and Mr. Joe Verhaeghe, for always being there when I needed them
- Finally, to my family, especially my parents for their constant love, support and encouragement throughout both my research, and my entire life.

TABLE OF CONTENTS

	page
ABSTRACT	(iii)
ACKNOWLEDGEMENTS	(iv)
TABLE OF CONTENTS	(v)
NOMENCLATURE	(vii)
LIST OF FIGURES	(x)
LIST OF TABLES	(xi)
1. INTRODUCTION	1
1.1 Velocity Measurement	1
1.2 Current Application of PIV	2
1.3 Objectives of the Present Work	3
2. LITERATURE SURVEY	4
2.1 Introduction	4
2.2 PIV System Components	6
2.2.1 Light Source and Optics	6
2.2.2 Light Scattering Medium	8
2.2.3 Recording Medium	15
2.2.4 Image Analysis	16
2.2.4.1 Direct Autocorrelation	16
2.2.4.2 Direct Cross-Correlation	19
2.2.4.3 Young's Fringes	21
2.2.5 Measurement Accuracy	22
2.3 Previous Experimental Work	24
2.3.1 Two-Dimensional Applications	25
2.3.2 Three-Dimensional Applications	31
2.3.3 Summary	35
2.4 Mixed Convection in Enclosures	36
3. EXPERIMENTAL SYSTEM	42
3.1 Experimental Apparatus	42
3.1.1 Test Cavity and Flow Loop	42
3.1.2 Light Source and Optics	45
3.1.3 Light Scattering Medium	48
3.1.4 Recording Medium	50
3.1.5 Image Analysis	51
3.1.6 Data Manipulation	52
3.2 Experimental Procedure	53
3.2.1 Preparation of Test Cavity	53
3.2.2 Preliminary Investigations	54

3.2.3	PIV Procedure	56
4.	RESULTS AND DISCUSSION	58
4.1	Introduction	58
4.2	Experimental Results	60
4.2.1	Qualitative Results	60
4.2.2	Quantitative Results	63
4.3	Comparison to Previous Work	72
4.4	Measurement Error	81
5.	CONCLUSIONS AND RECOMMENDATIONS	85
5.1	Conclusions	85
5.2	Recommendations	86
	REFERENCES	89
	APPENDICES	
A	Preliminary Investigations	92
A.1	Experimental Data	92
A.2	Calculations	93

NOMENCLATURE

a	Inlet ratio of cavity (see equation 2.26)
A	Cavity aspect ratio (see equation 2.27)
c	Algorithm accuracy parameter (see equation 2.20)
C	Mean number of particles per unit volume (see equation 2.8)
C_p	Specific heat of fluid at constant pressure (see equation 2.25)
d_e	Nominal image diameter (see equation 2.3)
d_f	Fringe spacing (see equation 2.18)
d_i	Diameter of interrogating beam (see equation 2.12)
d_p	Seeding particle diameter (see equation 2.1)
d_r	Resolution of recording medium (see equation 2.21)
d_s	Airy disk diameter (see equation 2.4)
d_r	Recorded image diameter (see equation 2.21)
D	Inlet height (see Figure 2.5)
D_H	Hydraulic diameter
D_o	Optical density (see equation 2.7)
E	Energy of light sheet (see equation 2.2)
$f(m,n)$	Brightness of first image (see equation 2.13)
f_i	Focal length of transform lens (see equation 2.18)
$f/No.$	Ratio of lens focal length to aperture (see equation 2.4)
$g(m,n)$	Brightness of second image (see equation 2.13)
g_i	Component of gravity acting on particle (see equation 2.29)
g_p	Particle acceleration (see equation 2.1)
Gr_L	Grashof number based on length scale, L (see equation 2.29)
H	Cavity height (see Figure 2.5)
I	Laser light intensity (see equation 2.9)
I_I	Laser light intensity of spot I (see equation 2.9)
k	Wave number (see equation 2.2)
K	Thermal conductivity of fluid (see equation 2.25)
l	Length characteristic (see equation 2.23)
l_i	Circumferential length of slot i (see equation A.2)
L	Length scale (see equation 2.28)
m	Horizontal image location (see equation 2.13)
m_r	Refractive index ratio (see equation 2.5)
M	Magnification of recording system (see equation 2.3)
n	Vertical image location (see equation 2.13)
n_L	Refractive index of fluid (see equation 2.5)
n_p	Refractive index of particle (see equation 2.5)
N	Number of revolutions/second of disk (see equation A.3)
$N_{chopper}$	Number of revolutions/minute of disk (see Table 3.1)
N_I	Image density of recording (see equation 2.12)
N_i	Data density (see equation 2.23)

N_s	Source density (see equation 2.8)
Pr	Fluid Prandtl number (see equation 2.25)
Q_{max}	Maximum volumetric flowrate of pump (see Table A.1 and A.2)
R	Radius of centerline of slot (see equation A.2)
$R(s)$	Autocorrelation of $I(X)$ (see equation 2.10)
R_{D+}	Positive displacement peak magnitude
R_{D-}	Negative displacement peak magnitude
R_p	Self-correlation peak magnitude
Re_L	Reynolds number based on length scale, L (see equation 2.28)
Ri	Richardson number (see equation 2.24)
s	Two-dimensional displacement vector (see equation 2.10)
$s(m,n)$	Spatial shift function (see equation 2.13)
t_i	Exposure time of slot i (see equation A.1)
t_r	Total exposure time (see equation A.5)
T_f	Film temperature (see Table 3.1)
T_j	Inlet jet temperature profile (see Figure 2.5)
T_w	Wall temperature (see Figure 2.5)
T_1	Cavity inlet temperature (see Table 3.1)
T_2	Cavity outlet temperature
u	Horizontal particle velocity component (see equation 2.19)
u_j	Horizontal inlet jet velocity (see equation 2.8)
u_{max}	full-scale horizontal velocity (see equation 2.22)
U	Dimensionless velocity (see equation 4.2)
v	Vertical particle velocity component (see equation 2.20)
\mathbf{v}	particle velocity vector (see equation 2.18)
v_d	Speed of rotation of disk (see equation A.3)
V	Dimensionless velocity (see equation 4.2)
W	Cavity width (see Figure 2.5)
x	Dimensional horizontal component (see Figure 3.2)
X	Dimensionless horizontal coordinate (see equation 4.1)
\bar{X}	Intensity coordinate (see equation 2.9)
\bar{X}_1	Centre of interrogation spot (see equation 2.9)
y	Dimensional vertical component (see Figure 3.2)
Y	Dimensionless vertical coordinate (see equation 4.1)
z	Dimensional horizontal component (see Figure 3.2)

Greek Variables

α	Dimensionless particle diameter (see equation 2.6)
α_L	Thermal diffusivity of fluid (see equation 2.25)
β	Coefficient of thermal expansion of fluid (see equation 2.29)
δt	Duration of light pulse
Δt	Separation time between exposures (see equation 2.11)
Δu_s	Particle slip velocity (see equation 2.1)

Δx	Displacement of particle (see equation 2.19)
Δx_{\max}	Maximum measured horizontal particle displacement (see equation 2.22)
Δx_0	Horizontal dimension of light sheet (see equation 2.2)
ΔX	Magnitude of displacement of particle image
Δy_0	Vertical dimension of light sheet (see equation 2.2)
Δz_0	Thickness of light sheet (see equation 2.8)
ε	Dissipation of turbulent kinetic energy (see equation 3.2)
$\bar{\varepsilon}$	Mean exposure of particle (see equation 2.2)
$\bar{\varepsilon}_0$	Fog level exposure
$\bar{\varepsilon}_{\min}$	Minimum exposure for creation of image
θ_i	Angle through which slot i sweeps (see equation A.2)
λ	Wavelength of incident light (see equation 2.2)
μ_{D+}	Centroid of positive displacement peak (see equation 2.11)
μ_l	Centroidal velocity (see equation 2.11)
μ_L	Dynamic viscosity of fluid (see equation 2.25)
ν_L	Kinematic viscosity of fluid (see equation 2.25)
ρ_L	Fluid density (see equation 3.1)
ρ_p	Particle density (see equation 2.1)
σ	Mie scattering cross-section of particle (see equation 2.2)
σ_i	Root mean square value of i (see equation 2.20)
σ_i^2	Mean square value of i (see equation 2.19)
τ	Intensity transmittance (see equation 2.7)
$\tau(\bar{X})$	Transmittance of photographic recording (see equation 2.9)
τ_k	Kolomolgorov turbulent fluctuation time scale (see equation 3.2)
τ_p	Particle time scale (see equation 3.1)
$\phi_{ff}(m,n)$	Autocorrelation function of f(m,n) (see equation 2.17)
$\phi_{fg}(m,n)$	Cross-correlation function (see equation 2.14)
Ω	Solid collection angle of system (see equation 2.2)

LIST OF FIGURES

	page	
2.1	General Optical Measurement System	5
2.2	Creation of Light Sheet by Cylindrical Lens	9
2.3	Particle Diameter vs. Dimensionless Exposure	13
2.4	Interrogation of a Photograph	17
2.5	Problem Specification	39
3.1	PIV System Schematic Diagram	43
3.2	Experimental Test Cavity	44
3.3	Experimental Flow Loop	46
3.4	Mechanical Chopping Disk	47
4.1	Observed Flow Regimes	61
4.2	Velocity Vector Grids	64
4.3	Case 1 PIV Results	66
4.4	Case 2 PIV Results	68
4.5	Case 3 PIV Results	70
4.6	Isothermal Flow - Vertical Velocity Near Heated Wall	74
4.7	Separated Flow - Vertical Velocity Profiles along Horizontal Centreline	75
4.8	Separated Flow - Vertical Velocity Profile Comparison	77
4.9	Separated Flow - Horizontal Velocity Profile Comparison	78
4.10	Buoyancy-Dominated Flow - Vertical Velocity Profiles along Horizontal Centreline	80
4.11	Buoyancy-Dominated Flow - Horizontal Velocity Profiles along Vertical Centreline	82

LIST OF TABLES

	page
3.1 Experimental Data	54
4.1 Summary of Cases	58
4.2 Summary of Dimensionless Experimental Separation Locations	76
4.3 Summary of Dimensionless Experimental Penetration Depths	81
A.1 Combinations investigated using 100 ASA colour film	92
A.2 Combinations investigated using p3200 ASA B & W film (f/No. = 1.8)	93

CHAPTER 1

INTRODUCTION

1.1 Velocity Measurement

Knowledge of characteristics such as velocity, temperature and density distributions is important in the design phase of practical applications involving fluid flow. Over the years, many methods have been developed to accurately measure these distributions. More specifically, the measurement of velocity distributions has been accomplished using invasive techniques such as hot wire anemometry. Unfortunately, invasive methods have one major drawback in that they disturb the flow which they are measuring, resulting in inaccurate measurements. Optical measurement methods do not share this problem. One such method, Laser Doppler Anemometry (LDA), has been used extensively to measure velocity fields in many different flow geometries because of its versatility and high accuracy, which ranges between 0.1 and 1 % [1]. However, data acquisition using LDA is extremely time-consuming as velocity measurements are made point-by-point. A consequence of this point-by-point nature, is that steady state conditions must be reached before measurements can be obtained, further increasing data acquisition time.

Qualitative information about velocity fields can be obtained using flow visualization techniques such as dye tracers, schlieren photography and streak photography. Used to estimate quantitative data (e.g. velocity), they perform about one order of magnitude worse than single-point methods (1 to 10% accuracy). A class of optical measurement techniques which combines the accuracy of single-point methods with the multi-point nature of qualitative

flow visualization, is Pulsed Laser Velocimetry. These techniques record optical images of neutrally-buoyant flow tracers and deduce the velocity fields from the displacement of the flow tracers during short time intervals. The development and optimization of these techniques has been made possible by advances in image processing technology and improved computer hardware. Using these methods, an instantaneous measurement of the entire flow field is taken non-invasively, which markedly reduces data acquisition time and increases measurement accuracy. The instantaneous nature of these techniques allows measurement of velocity fields where unsteady conditions exist. Such measurements are often difficult to obtain using single-point methods.

The two general methodologies in this class of velocity measurement techniques are Laser Speckle Velocimetry (LSV) and Particle Image Velocimetry (PIV). PIV was chosen for study in this work because it has been used less extensively than LSV, and the need for improvement still exists. It is hoped that this work will aid in its development as a useful velocity measurement tool.

1.2 Current Application of PIV

In the current investigation, the PIV technique is applied to mixed convection in rectangular enclosures, previously studied both experimentally and numerically by Nurnberg [2]. In his work, he developed a numerical code which predicted the velocity and temperature distributions within a rectangular enclosure (see Figure 3.2). The working fluid used was water, and a temperature gradient was provided by heating one vertical wall. Experimental investigations were performed for a number of cases, varying both the inlet jet velocity and the temperature of the heated wall. For each case, the steady-state velocity distribution was measured using LDA and the corresponding temperature distribution was

measured using invasive thermocouple probes. Using these measurements, he was able to verify the performance of the numerical code, and concluded that the code accurately predicts velocity and temperature distributions for this enclosure. Relevant mixed convection theory and more information about these investigations are presented in the literature survey (Section 2.4).

1.3 Objectives of the Present Work

The objectives of the present work are two-fold. First, since LDA has been proven to be an accurate measurement technique, comparing results of the present work to those obtained by Nurnberg using LDA will determine the performance of the PIV technique as an accurate measurement tool. Following this, if the results obtained using the two techniques are consistent, the PIV results can be used to further verify the velocity distributions predicted by Nurnberg's [2] numerical code. An inexpensive PIV system consisting of readily-available components is assembled to perform the current investigation. After determining the performance of PIV as a measurement tool, and with the knowledge gained in performing the experiments, recommendations are made for the assembly of a superior system for use in the future.

CHAPTER 2

LITERATURE SURVEY

2.1 Introduction

In general, an optical measurement system consists of a source of light, a coding method which modulates the light in space or in time, markers in the flow field, a recording medium to sense light from the markers, and a system for analysing the information on the recording medium [1]. Figure 2.1 shows a schematic diagram of the general optical velocity measurement system. In PLV, the flow is illuminated by a strong light source and the particle positions are recorded by imaging the light scattered by the particles onto a recording medium. PLV is performed primarily with double-pulsed sheet illumination, but it can be done with multiple pulses or with volume illumination and holographic recording [1]. The two general methodologies of PLV are Laser Speckle Velocimetry (LSV) and Particle Image Velocimetry (PIV). If the particle concentration is high, speckle patterns will be formed by random interference of light scattered from many randomly located scattering sites [1]. The fundamental concept of LSV is that the speckle pattern translates with the scattering sites that create it, so that measurement of the speckle motion is equivalent to measurement of the scattering site motion. Displacement can be determined by recording a double-exposure photograph of the speckle pattern associated with a moving body. When the particle concentration is low, individual particles are imaged, and their displacements are similarly recorded on double-exposure photographs. By measuring the displacement of the speckle pattern or the individual particle, its velocity magnitude can subsequently be found by dividing its displacement by the separation time

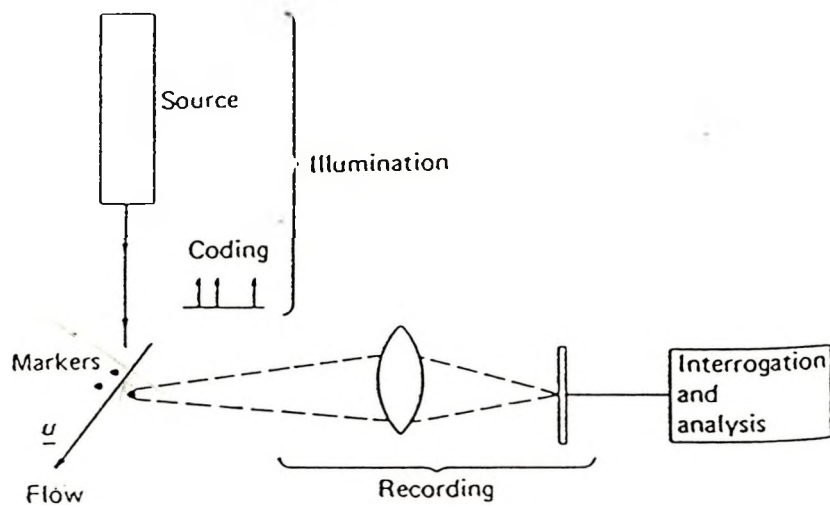


Figure 2.1 - General Optical Measurement System [1]

between the two exposures. Determining the direction of the particle's velocity vector is somewhat more difficult, and depends on the method of image analysis used. By determining the velocity vector for each particle in the flow field, the entire velocity field can be inferred from particle movements. LSV has been used extensively in the past, however it requires a time-consuming image analysis technique. With advances in computer technology, PIV has evolved into a superior technique requiring less time for data analysis while maintaining high measurement accuracy. The current investigation was performed using PIV for these reasons.

The first section of this chapter describes the components that comprise the PIV system, with one subsection focusing on the uncertainty encountered in PIV experiments. Following this, a section is devoted to providing illustrative examples of applications of the PIV technique. The third and final section in this chapter provides a brief review of the theory involved in mixed convection experiments.

2.2 PIV System Components

2.2.1 Light Source and Optics

A deciding factor in choosing a source of light for a flow imaging experiment is whether it will provide sufficient intensity such that the particles will be detected in the image plane. The sensitivity of the image recording medium and the scattering power of the seeding particles will also play a role in this decision. Although many different sources of light have been used in past experiments, such as flashlamps and strobe lights, the most widely used light source is the laser. Laser light possesses four qualities which make it ideal for use in PIV. These are its directionality, temporal and spatial coherence, intensity and monochromaticity. Both the continuous wave and pulsed laser have been used in the past, however the latter has been used more extensively as it can produce very short, well-defined pulses of highly intense light, with

small separation time between pulses. This characteristic is required for accurate PIV measurements so that clean, bright images of moving particles can be obtained, rather than particle streaks. The minimum pulse duration a laser can produce will be the limiting factor as to the maximum flow velocity that can be determined. The ability of a pulsed laser to respond rapidly to an initiating trigger and its flexibility in varying the duration and frequency of the light pulses make it ideal for PIV experiments. However, pulsed lasers are typically very costly, both to purchase initially and also to maintain, as they usually require additional equipment for cooling, and modifications to standard power supply. Pulsed lasers can produce short pulses by two different methods. Excitation of the lasing medium can be provided by a flashlamp, or alternatively, a technique called "Q-switching" can be used. Q-switching, called this because it changes the "quality factor" in the laser cavity, suppresses the gain in the resonator so the power can be stored in the laser medium, then quickly increases the cavity quality factor so the laser emits the accumulated energy in a short pulse. Although Q-switching provides shorter pulses (nanosecond range) than flashlamp excitation (milli- to microsecond range), the intensity of the pulse is not as high. As a cheaper and simpler alternative to the pulsed laser, light emitted by a continuous wave laser may be interrupted by optical or mechanical means to create short pulses, with only a slight loss in accuracy.

Using either a pulsed laser or a chopped continuous source the incident light is interrupted to create a pulse code. In double-exposure PIV, the primary function of a pulse code is to provide images at two precisely determined times, separated by Δt , from which the displacement can be measured [3]. The code can also provide additional information such as direction of the flow. The separation time Δt is the single most important adjustable parameter in a PIV system, as it determines the maximum and minimum velocities that can be measured, i.e. the dynamic range of the system [3]. The duration of the light pulse, δt , determines the degree to which an

image is frozen during the exposure. To avoid blurring of the image, the value of $\delta t/\Delta t$ should be kept small [3].

In most two-dimensional applications, the laser light is focused into an intense light sheet to investigate the velocity field in a single plane approximately 1 to 5 mm thick. Sheet illumination permits a greater number of particles per unit area in the sheet, and hence greater velocity information in the plane [1]. A two-dimensional plane of light can be created by placing a cylindrical lens in the path of the laser beam, as shown in Figure 2.2. The beam expands in one plane only, producing a sheet of light whose thickness is approximately equal to the diameter of the incident laser beam [4]. Three-dimensional measurements, which require volume illumination can also be made, however this aspect of PIV is beyond the scope of this project. Some examples of three-dimensional PIV will be given in a later section to demonstrate the versatile nature of the technique.

2.2.2 Light Scattering Medium

In the PIV system, the presence of a light scattering medium in a flow field allows the determination of the velocity field. To determine this velocity field from the movement of particles within it, it is required that the particles follow the flow accurately. This requires that the particles be neutrally buoyant and as small as possible so that the slip velocity between particle and fluid is a minimum. Buchhave [5] suggests that the basic tool to evaluate the particle size requirement is Stokes's law, which connects the particle slip velocity Δu_s and the resulting force on the particle:

$$\Delta u_s = g_p d_p^2 \rho_p / 18\mu_L \quad (2.1)$$

where g_p is the particle acceleration, d_p and ρ_p are particle diameter and density respectively, and μ_L is the dynamic viscosity of the fluid. Since Δu_s is strongly dependent on d_p , it is readily

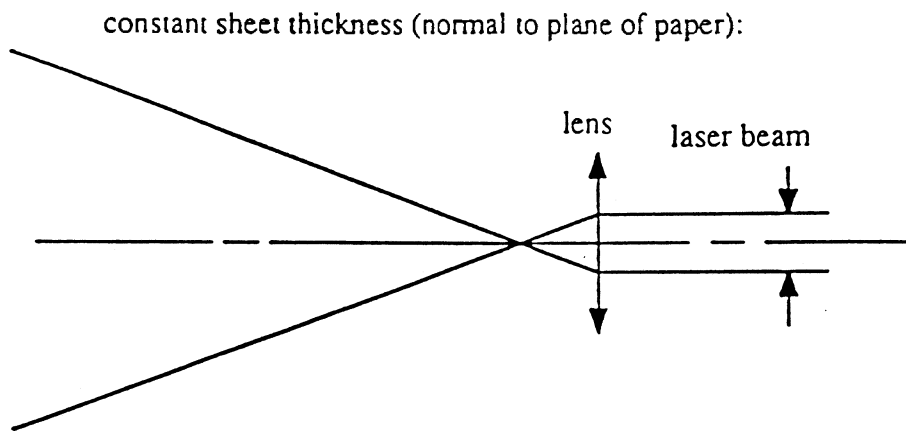


Figure 2.2 - Creation of Light Sheet by Cylindrical Lens [4]

apparent that d_p should be kept as small as possible to minimize the slip between particle and fluid. This will ensure accurate determination of the velocity field from particle movement. Images of small particles are desirable because the accuracy of velocity measurements and the spatial resolution improve with decreasing image diameter [6]. However, the main requirement of PIV is the production of high-resolution, high-contrast recordings of particle positions [5]. Thus, using larger particles would be beneficial as they are more readily detected by the imaging system since they scatter more light. This would also decrease the intensity of light needed to produce quality images, thereby reducing the cost of the light source. Therefore, the optimum particle size is a compromise between the requirement that the particles follow the flow and the need for enough scattered light to create a particle image of sufficient quality [5].

The selection of an appropriate scattering medium depends on the nature of the working fluid, i.e. density, working temperature, state, as well as the intensity of incident light available for scattering, and the sensitivity of the recording medium. Using smaller particles, thereby allowing higher accuracy and data density, is possible when the light source is a pulsed laser, since it achieves high pulse intensity by concentrating the energy into a short pulse. Chopped continuous sources do not enjoy this benefit; moreover, as the flow rate and the chopping rate increase, the pulse duration and hence the energy per pulse decrease in inverse proportion, limiting these light sources to relatively slow flows and/or large particles, unless the detector is very sensitive [3].

Adrian and Yao [6] investigated the scattering properties of various particles. Assuming monodisperse particle populations (e.g. constant diameter), and using Mie's theory for scattering from spherical particles to evaluate the exposure produced on a photographic plate during a laser pulse, they were able to determine the minimum particle diameter required for successful PIV in water and air for various types of particle and various film properties. Following is a brief

description of their work. The ability of a recording medium to detect a particle depends on the exposure, $\bar{\epsilon}$, of its image which is defined as the energy density in the image plane, i.e. the energy per unit area incident on the imaging device. The mean exposure for a particle in a uniform light sheet of energy E , with dimensions $\Delta x_0 \times \Delta y_0$ is given by:

$$\bar{\epsilon} = \frac{4}{\pi k^2 d_e^2} \frac{E}{\Delta x_0 \Delta y_0} \int_{\Omega} \sigma^2 d\Omega \quad (2.2)$$

where $k=2\pi/\lambda$ is the wave number, λ is the wavelength of the incident light, Ω is the solid collection angle of the lens system, σ is the Mie scattering cross-section of the particle, and d_e is the nominal image diameter, defined by:

$$d_e = \sqrt{M^2 d_p^2 + d_s^2} \quad (2.3)$$

where M is the magnification of the recording system and d_p is the particle diameter. In this equation, d_s is the diameter of the point response function of a diffraction-limited lens measured at the first dark ring of the Airy disk intensity distribution, defined by:

$$d_s = 2.44(M+1)f/No.\lambda \quad (2.4)$$

where $f/No.$ is the ratio of lens focal length to aperture diameter. Equation 2.3 approximately represents the combined effects of magnification and image blurring in determining the final diameter of the image. The scattering integral in equation 2.2 was calculated by Adrian and Yao [6], using Mie's scattering theory assuming homogeneous spherical particles. The scattering results were found to depend on m_r , which is the ratio of the refractive index of the particle, n_p , to the refractive index of the fluid n_L , given by:

$$m_r = n_p / n_L \quad (2.5)$$

and the dimensionless particle diameter defined as:

$$\alpha = \frac{\pi}{\lambda} d_p \quad (2.6)$$

Results of interest to the current experiment are those for polystyrene particles with a refractive index of 1.59, in water. Figure 2.3 shows these results in a generated family of curves of mean exposure versus particle diameter for varying values of $f/No.$ A non-dimensional mean exposure is plotted, which is the calculated exposure (energy density in the image plane) divided by the energy density of the laser sheet. In their calculations, a ruby laser ($\lambda=694.3$ nm) was used which provided a pulse of 2.546 J distributed over a light sheet with an area of 100 mm². In this figure, D_o is the optical density defined as:

$$D_o = \log_{10}(1/\tau) \quad (2.7)$$

where τ is the intensity transmittance, defined as the ratio of light transmitted to the image plane to the incident light. For photographic film, the common criteria for the recording of a successful image is that the mean exposure must exceed some multiple of the "fog" level exposure $\bar{\epsilon}_o$. Below this level the transmissivity is independent of the incident intensity. According to Adrian and Yao [6], $D_o=1$ is considered to be a clean image, which corresponds to $\bar{\epsilon}_{min}=1.52$ mJ/m² for Technical Pan 2415 film. The information in Figure 2.3 indicates that for larger values of $f/No.$, particles in the range of 1-5 μm can be used, and a diameter of 10 μm is acceptable for smaller values of $f/No.$ This value of $\bar{\epsilon}_{min}$ can be compared to that found by Walter and Chen [4], who used a CCD (Charge-Coupled Device) camera for their PIV experiments. They found $\bar{\epsilon}_{min}$ to be 6.88×10^{-4} mJ/m², which reveals that the CCD camera is three times more sensitive than typical photographic film. It would seem that a CCD camera is particularly well suited to PIV experiments, which take place at low light levels. By modifying the results of Adrian and Yao to suit their experiment, Walter and Chen [4] estimated that their CCD camera would be capable of imaging particles as small as 1 μm , using a much less powerful

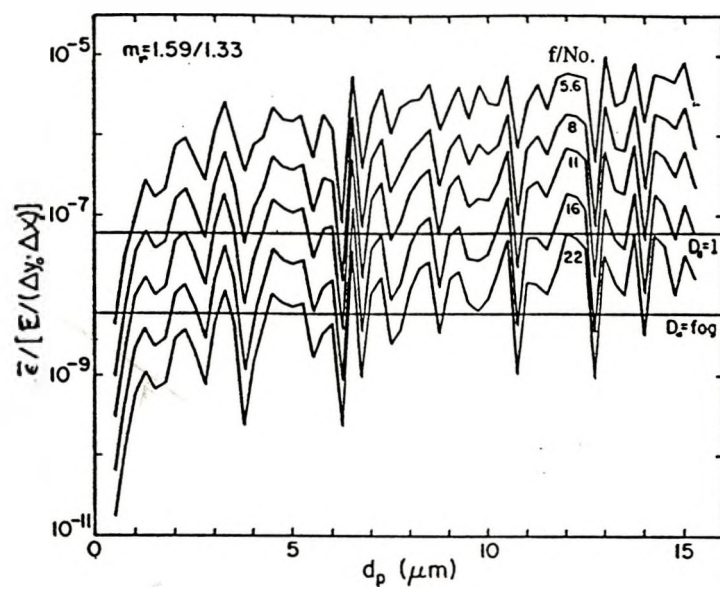


Figure 2.3 - Particle diameter vs. dimensionless exposure for polystyrene particles in water at $\lambda = 694.3$ nm using Kodak Technical Pan [6]

He-Ne laser for illumination. However, using the above equations it was found that there is no optical advantage in attempting to image particles smaller than $250 \mu\text{m}$ due to the relatively coarse resolution of the CCD camera. In other words, images of particles smaller than this will still occupy at least one pixel, which would not increase the spatial resolution of the recording. Applying the above equations to the current experimental set-up, it was found that the lower limit of particle diameter for the camera resolution is approximately $89 \mu\text{m}$. A more detailed discussion of the operation and characteristics of the CCD camera is presented in the following section and the next chapter. This comparison simply shows the superiority of the CCD camera over photographic film in the area of sensitivity. This characteristic is important to consider when choosing the diameter of seeding particles to be used.

Examining equation 2.2, Adrian [3] found (somewhat surprisingly) that as the particle size increases into the geometric scattering regime, the image intensity of a particle becomes independent of the particle diameter, because both the scattered light energy and the image area increase as d_p^2 . Thus beyond a certain size, of order $100 \mu\text{m}$, there is little to be gained by using larger particles.

The concentration of seeding particles per unit volume, C , determines both the mode of operation of the velocimeter, and the accuracy of the velocity measurements which will be discussed in section 2.2.5. A dimensionless parameter called the source density can be defined:[1]

$$N_s \equiv C\Delta z_0 \pi d_c^2 / 4M^2 \quad (2.8)$$

where Δz_0 is the thickness of the laser sheet, d_c is defined in equation 2.3 and M is the magnification of the recording system. If $N_s \gg 1$, laser speckle appears; if $N_s \ll 1$, individual particle images are recorded.

2.2.3 Recording Medium

Two-dimensional recordings of particle movement can be made using photographic film, photographic plates, or cinematic recording including high speed cameras, video cameras and solid-state image sensors [1]. The principal difference between film and video is the spatial resolution each can provide. Film offers much higher resolution, and thus tends to be used for high-resolution and wide dynamic velocity range measurements of fluids, whereas video recording is suitable for lower resolution, lower accuracy flow measurements, for higher accuracy measurements over smaller fields of view, or for measurements of larger particles in two-phase flow [3]. One important advantage of video over film is the ease with which images can be digitized for storage and manipulation on a computer. Normally images are analysed using a computer equipped with an A/D board (frame grabber), which digitizes individual video frames for immediate analysis. Using this medium, results from an experiment can be obtained very quickly, and it can be determined whether further experiments need be performed. However, analysis of images on photographic film or plates requires development of the film, and an interrogation technique which is very time-consuming and requires additional optical equipment. So although photographic film offers greater resolution, approximately eight times that of a video recording, video cameras offer a more flexible means of data acquisition and storage [4].

A solid-state device that is used frequently in PIV experiments is a video camera equipped with a CCD (Charge-Coupled Device). It has been chosen over other recording media because of its high sensitivity at low light levels and its large dynamic range, which is the ratio of intensities of the brightest object that can be imaged to the dimmest. The CCD camera eliminates the need for film development, and when used in real-time, eliminates the need for a digitizer as digitization is accomplished by the CCD chip. Clearly, the CCD camera is an ideal choice for use in PIV experiments.

2.2.4 Image Analysis

The method of image analysis used to obtain the velocity field from a PIV image depends upon the type of recording medium used. The methods of interrogation that are currently in use are primarily statistical approaches that probabilistically infer the proper pairings and measure the average displacement of a group of particles within a given interrogation spot [3]. As shown in Figure 2.4 (top), interrogation is begun by illuminating an interrogation spot with an unexpanded laser beam of intensity $I_1(\bar{X}-\bar{X}_1)$, where \bar{X}_1 is the centre of the spot. The interrogation spot intensity is given by:

$$I(\bar{X})=I_1(\bar{X}-\bar{X}_1)\tau(\bar{X}) \quad (2.9)$$

where $\tau(\bar{X})$ is the transmissivity of the photographic image. If the images are recorded on a video frame instead of photographic film, the interrogation spot can be defined digitally by multiplying the data in the frame array by a window function whose shape corresponds to that of an interrogating beam (I_1).

The following interrogation techniques provide the most probable displacement of a group of particles within the interrogation spot or window. Most of the theory presented here is taken from [3].

2.2.4.1 Direct Autocorrelation

The autocorrelation of $I(\bar{X})$ is given by:

$$R(s) = \int_{spot} I(\bar{X})I(\bar{X}+s)d\bar{X} \quad (2.10)$$

where s is a two-dimensional displacement vector. Where $s=0$ there exists strong self-correlation peak R_p , corresponding to each image correlating with itself. A second peak, R_{D+} exists where

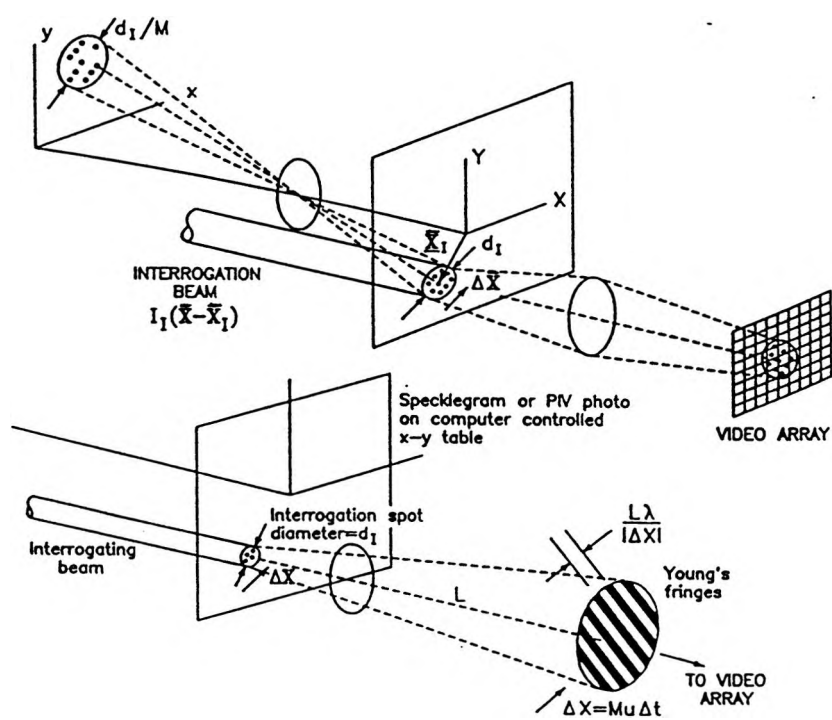


Figure 2.4 - Interrogation of a photograph. (Top) Direct image digitization; (Bottom) Young's fringe method in which a lens performs an optical two-dimensional Fourier transform of the image field in the interrogation spot. [3]

s equals the mean displacement. This is called the positive displacement peak, and corresponds to first images correlating with second images. An identical peak R_D occurs at the negative value of the mean displacement, corresponding to second images correlating with first images. In addition to the self-correlation peak which defines the origin, and the two strong displacement peaks, there are a number of noise peaks resulting from the random overlap of particle images in the $I(\bar{X})I(\bar{X}+s)$ product. The velocity is then determined by locating the centroid of the tallest peak in the correlation plane (other than the self-correlation peak). If the tallest peak is the positive displacement peak with centroid μ_{D+} , then the velocity is estimated by:

$$\mu_I = \frac{\mu_{D+}}{M\Delta t} \quad (2.11)$$

The strength of the displacement correlation peak is proportional to the number of particle-image pairs within the interrogation spot. This number is proportional to the particle seeding density, decreased by the fraction of second images that leave the interrogation spot due to out-of-plane motion and the fraction lost by in-plane motion. As the velocity increases, fewer image pairs exist within the interrogation spot and the displacement correlation peak becomes smaller and less likely to be detected. This is referred to as *velocity bias*. Velocity bias is much less severe when the particle seeding density is high because the number of remaining image pairs is large enough to prevent measurement failure. If the image density of a recording is defined as:

$$N_I = C\Delta z_o \pi d_i^2 / 4M^2 \quad (2.12)$$

where C , Δz_o and M are defined as for equation 2.8 and d_i is the diameter of the interrogation spot, then it can be said that the fraction of successful measurements obtained from such a recording asymptotically approaches 100% as N_I becomes large and $|\Delta X|/d_i$ is made small. ΔX is the displacement of the particle image between exposures.

2.2.4.2 Direct Cross-correlation

The loss of pairs due to in-plane motion out of the interrogation spot can be eliminated by performing cross-correlation between first images in a small, first interrogation window and second images in a larger, second interrogation window. The second window is chosen on the basis of prior knowledge about the flow field, such as predominant mean flow, an imposed image shift, or an estimate of the local flow direction based on neighbouring vectors. Cross-correlating images in a first interrogation spot with those in a second spot will increase the strength of the correlation peak and thereby increase the probability of making valid measurements. The use of this technique can be illustrated by the image analysis performed by Chen et al. [7], who investigated velocity fields in a cubic chamber with an offset inlet and outlet. In their analysis, a linear system is used to model the space-shift (displacement) information of two sequential digitized flow images, which can be expressed as:

$$g(m,n) = [f(m,n) * s(m,n)] \quad (2.13)$$

where $f(m,n)$, denotes the brightness of the input (first) digital image at pixel location (m,n) , $g(m,n)$ denotes the brightness of the corresponding output (second) digital image, and $s(m,n)$ denotes the spatial shift function. The symbol $*$ denotes the spatial convolution of the two functions. If the space shift function reveals the probability distribution of the displacement information between the two sequential images, then its maximum stands for the most probable displacement of the particles between the first and second images. To find the shift function, the spatial cross-correlation function between the images is computed, and its maximum is located. Mathematically, the cross-correlation function ϕ_{fg} of the sampled region (in this case 30 x 30 pixels), is equivalent to the expectation operated on the $f(m,n)$ and $g(m,n)$ [8]:

$$\phi_{fg}(m,n) = E[f(m,n),g(m,n)] \quad (2.14)$$

By definition the expected value is expressed as:

$$E[f(m,n),g(m,n)] = \int_{k=-\infty}^{+\infty} \int_{l=-\infty}^{+\infty} f(m,n)g(k+m,l+n)dldk \quad (2.15)$$

Physically, the cross-correlation function ϕ_{fg} reveals the degree of matching between particles of initial and shifted images in the sampled region. In statistical form, the cross-correlation function is the expectation operation on the initial and shifted spatial signals:

$$\phi_{fg}(m,n) = E[f(m,n),f(m,n) * s(m,n)] \quad (2.16)$$

This can be expanded to:

$$\phi_{fg}(m,n) = \phi_{ff}(m,n) * s(m,n) \quad (2.17)$$

where $\phi_{ff}(m,n)$ is the autocorrelation function of the input function $f(m,n)$. Since the input function $f(m,n)$ correlates with itself in $\phi_{ff}(m,n)$, the maximum of the autocorrelation function is always located at the origin of the cross-correlation domain. The origin is therefore the initial position of all particles within the sampled subregion. The purpose of equation 2.17 is to move the autocorrelation peak away from the origin by the average spatial displacement of particles in the sampled region. The values of $\phi_{fg}(m,n)$ in the sampled region of two sequential images are calculated. Then once the maximum value of $\phi_{fg}(m,n)$ within the region is determined, the shift function $s(m,n)$ is found by measuring the distance between the origin and the location of the maximum value of $\phi_{fg}(m,n)$. Given the time interval between the two images the velocity vector at the sampled region is then determined. The velocity field is obtained by repeating this procedure on other sample regions until the entire digitized flow image has been interrogated.

2.2.4.3 Young's Fringes

The Young's fringe method has been the most widely used technique for interrogating PIV images recorded on photographic film [3]. As shown in Figure 2.4 (bottom), an unexpanded laser beam is passed through the processed film, where each image in the interrogation spot acts as a point source whose rays are collimated by the lens into a plane wave propagating at a small angle to the optic axis of the lens. Each pair of images produces a pair of mutually inclined plane waves that interfere to form a Young's fringe pattern oriented perpendicular to the displacement vector between the images. The pairs that are separated by the same displacement vector form identical fringes that reinforce each other, thereby creating a dominant pattern [3]. The lens placed after the film performs an accurate, two-dimensional Fourier transform of the phase and amplitude of the light wave if it is located one focal length from the film, and if the fringe plane is located one focal length from the lens [3]. The magnitude of the particle's velocity can then be found by [9]:

$$|v| = \lambda f_l / M d_f \Delta t \quad (2.18)$$

where	λ	is the wavelength of the interrogating laser beam
	f_l	is the focal length of the transform lens placed after the film
	M	is the optical magnification of the recording system
	Δt	is the time between laser pulses
and	d_f	is the perpendicular distance between adjacent fringes.

The direction of the particle's displacement is perpendicular to that of the fringes, however an ambiguity of 180 degrees exists in the determination of the velocity vector. To determine the fringe spacing and orientation, the fringe pattern is digitized by a video camera, and a fast Fourier transform (FFT) of the digitized array is then calculated by a computer. The FFT of the fringe intensity will yield a convolution function that contains a self-correlation peak, positive and negative displacement peaks and noise peaks. The fringe spacing d_f is determined from the

positive displacement peak as in the other methods, and the velocity is calculated using equation 2.18. The main disadvantage of this interrogation method is that it requires development of the film, and therefore real-time measurements cannot be made.

2.2.5 Measurement Accuracy

Determining the effectiveness of PIV as a useful measurement tool requires validation of its resolution, accuracy, range and an understanding of biases inherent in the method [10].

The accuracy of velocity measurements obtained using the PIV technique depends on the ability to determine the displacement of the particle, Δx over a certain time interval from measurements of displacement of the particle's image, ΔX [3]. Assuming for simplicity, one-dimensional motion of velocity u , $\Delta x = M\Delta X = Mu\Delta t$ and:

$$\frac{\sigma_u^2}{u^2} = \frac{\sigma_{\Delta x}^2}{\Delta x^2} + \frac{\sigma_{\Delta t}^2}{\Delta t^2} \quad (2.19)$$

where σ^2 denotes the mean square value of the error in measuring the subscript quantity. Uncertainties in Δx arise in locating the appropriate reference points on the particle images used to mark the beginning and end of the displacement, i.e. the location of the first and second images. The reference point is usually taken to be the centroid of the particle image. Errors in determining the centroid of an image arise from irregularities in image shape, finite resolution due to recording the image on film of finite grain size or a video array of finite pixel size, and/or noise in the electronic readout of the video camera [3]. For most of these errors the rms value of Δx is proportional to the length of the image given by the sum of the recorded image diameter, d , and blur due to particle translation during exposure [3]:

$$\sigma_{\Delta x} = c[d_r + M(u^2 + v^2\delta t)^{1/2}] \quad (2.20)$$

where u and v are the respective horizontal and vertical components of the particle's velocity, c

is a number which depends on the accuracy of the algorithm used to determine image centroid location and d_i is the recorded image diameter defined as:

$$d_r = \sqrt{Md_p^2 + d_s^2 + d_r^2} \quad (2.21)$$

where d_s is given by equation 2.4, and d_r is the resolution of the recording medium. The uncertainty in Δt and blur depend on the light source, but this is usually small unless the flow speed is very high.

Using these assumptions, Adrian [1] reduced equation 2.19 to the following, expressing the accuracy of the velocity measurement as a fraction of the full-scale velocity u_{\max} :

$$\frac{\sigma_u}{u_{\max}} = c \frac{d_r}{\Delta x_{\max}} \quad (2.22)$$

wherein $\Delta x_{\max} = u_{\max} \Delta t$, is the spatial uncertainty in the location of the velocity measurement, fixed by the maximum velocity range spanned by the PIV system. This shows that good accuracy necessitates the use of smaller particle images, i.e. smaller particles. Good spatial resolution is achieved by limiting the displacement of the marker and good accuracy is possible if the image diameter, d_r is small as compared to the displacement [1]. To be comparable with the spatial resolution of hot wire and laser-Doppler anemometry, Δx_{\max} should be of the order of 1 mm or less which requires a very small separation time when the velocity is high, necessitating the use of a high-powered pulsed laser [1].

The amount of information contained in a recording depends on the number of particles per unit volume, C . The concentration should be large enough to resolve thin fluid layers within the flow, i.e. internal shear layers and viscous boundary layers [1]. To quantify the amount of data contained on a recording, a dimensionless data density is defined [1]:

$$N_l \equiv Cl^3 \quad (2.23)$$

where l is a length characteristic of the thin fluid layers. When N_l is large the markers provide data at many points within the small scales of the flow and the fluid motion is resolved. However when N_l is small it is not possible to resolve all of the scales but large scale motion may be observed. Although any smooth field can be obtained by interpolation of randomly sampled data points, the results will be inaccurate unless $N_l \gg 1$ [3]. Measurement accuracy also depends on a second dimensionless parameter called the image density as defined in equation 2.12. This value characterizes the number of images within an interrogation spot on a two-dimensional recording medium. When N_l is large, each interrogation spot contains many images on average and therefore each spot is capable of yielding an accurate velocity measurement. When $N_l \ll 1$ the fraction of spots that yield data is approximately N_l . High image density implies a high data density if Δz_0 and d_l are of order l or smaller, and good measurements are possible under these conditions.[1,3] Thus, the high-image-density limit maximizes the spatial resolution of PIV [3].

2.3 Previous Experimental Work

Particle image velocimetry has been used to measure two-dimensional velocity fields in a variety of applications involving gas, liquid and two-phase flows. Recent advances in optical and computer technology have made three-dimensional measurements possible, and it is suspected that future technological advances will simplify data acquisition, improve measurement accuracy, and shorten data analysis time. A number of two-dimensional applications will be presented which illustrate the adaptability of PIV to different flow conditions. Although three-dimensional measurements are beyond the scope of this project, some examples will be given to illustrate the expanding, versatile nature of PIV.

2.3.1 Two-dimensional Applications

Generally, two-dimensional PIV is applied to those situations where the flow pattern is simple. It can then be assumed that one plane of the flow is identical to all other planes. The PIV technique is particularly suited to 2-D flows as it allows the measurement of the in-plane velocity components, only if the out-of-plane component is small. Otherwise there is a substantial loss of correlation in the recording due to particles moving out of the illuminated plane during the separation time between exposures [11].

Dong et al. [12] used PIV to perform an analysis of the flow within the volute of a centrifugal pump. The beam of a frequency-doubled, pulsed Nd:Yag laser was expanded to a 1 mm thick light sheet by a combination of cylindrical and spherical lenses. This sheet could then be used to illuminate any desired section of the volute through its transparent perimeter. Particles with specific gravity varying between 0.95 and 1.05 and containing imbedded fluorescent dyes that respond efficiently to green laser light, were manufactured by the authors especially for these experiments. Three pulses of the laser were used to record three images of these particles on a single frame of a camera with its focal axis located at 90° to the direction of the light sheet plane. A negative of the images was illuminated from behind and examined by a video camera equipped with a microscopic objective. The video image was then fed to a computer where it was digitized and the autocorrelation method was used to determine the mean shift and the velocity of particles within many small interrogation windows that comprised the entire image. By measuring velocity distributions at different impeller blade orientations and flow conditions, PIV measurements provided information about circumferential, radial and axial variations in the velocity distribution, conservation of angular momentum on and off design conditions, the extent of a jet/wake phenomenon, the effect of blade orientation on the velocity and overall flux, the extent of leakage between the tongue and the impeller and the significance of turbulent stresses and dissipation on

the energy and angular momentum of the fluid. Information of this type was previously very limited and therefore certain assumptions were often made to model volute flow. The results of these experiments were used to evaluate the validity of these typically made assumptions.

Hassan and Blanchat [13] constructed a flow facility to allow measurement of a low Reynolds number jet, recirculations, and two-phase dispersed bubble flow. A system of mirrors and cylindrical lenses shaped the beam from a frequency-doubled, high-energy Nd:Yag laser into a light sheet approximately 1 mm thick. A synchronization circuit for the high-energy laser and the imaging system was constructed so that each time the laser pulsed, a separate image was recorded. The recording medium used was a high-resolution Vidicon camera which digitized the image directly. This camera was equipped with a 1024 x 1024 pixel array which allowed larger areas to be viewed with the same resolution as smaller areas with high resolution. Image analysis was accomplished by using a particle tracking code developed by Hassan et al. [14], which performed a direct point-by-point matching of images from one frame to the next. The result of this code was a set of data that was plotted to give the images in each track, the starting frame of each track, and the length of the track. These tracks were plotted as velocity vectors whose magnitudes and direction could then be viewed as quantitative or qualitative velocity vectors for the flow in question. Reasonable agreement was obtained when quantitative results of particle seeded flow (6 μm latex spheres) were compared to computer simulations and composite images comprised of a number of overlaid consecutive images. Overlaying consecutive images of dispersed bubble flow produced a "streak" track which made it relatively easy to visually track the flow with little ambiguity. Good correlation was found between the "streak pictures" and the corresponding particle velocity plots determined by the tracking code.

This same system and particle tracking code were used by Hassan et al. [15] to measure both components of a two-phase flow. In this study, dispersed air bubbly flow and its effects

upon a surrounding working fluid of mineral oil were investigated. The test section consisted of an open-top rectangular enclosure, with an air inlet flow line through its base. In order to quantify velocity fields of both components of the two-phase flow, each component had to be appropriately seeded. The working fluid was seeded with $70\ \mu\text{m}$ plastic spheres having a specific gravity of 1.02, and air bubbles produced from the tip of a 27-gauge surgical needle, served as natural seeding for the gaseous component. Full-field instantaneous velocity profiles of both liquid and gaseous components were obtained, as well as the temporal velocity fluctuation of the liquid phase induced by the rising bubble motion at a given point. It was found that seed particles were upwardly entrained within the wakes of passing bubbles. The estimated relative error in velocity measurement was 10 - 50 %, based on the fact that the error was proportional to the inverse of the particle displacement between exposures. From this, it could be suggested that the time between exposures should be chosen so that the particle's displacement is as small as possible, while remaining large enough for accurate measurement. This application of PIV demonstrates its potential for use in the further detailed study of multi-component flows, specifically in regards to its ability to quantify relative component velocities, upon which parameters such as interfacial drag and flow regime characterization are dependent. The PIV technique could assist in the development of a complete understanding of two-phase flows.

Kim and Chen [16] performed a PIV investigation of the flow within a cavity with a rotating upper surface. The basic geometry was a cylindrical cavity with the top lid driven to rotate at a steady angular rotation of 10 rpm. A 2 W Argon laser and a rectangular cylindrical lens were used to create a horizontally oriented light sheet which was thick enough ($> 2.5\ \text{mm}$) to capture the radial and axial motion in the test section. Particles with a mean diameter ranging from $50 - 100\ \mu\text{m}$, and a specific gravity of 1.03 were scattered throughout the test section, and their images were recorded by a CCD camera. Each camera frame contained a single-exposure

image, so that given a small interrogating window, many velocity vectors could be drawn between two temporally successive images by linking any two particle's images, from the initial to the following image. Their method of determining velocity vectors is quite similar in concept to the statistical correlation proposed by Willert and Gharib [8]. (see Section 2.2.4.2) To verify velocity fields obtained in the PIV experiment, Kim and Chen [16] performed a numerical simulation of the lid-driven rotating flow. When compared to the laminar numerical results, the experimental results were in good agreement, with the exception of small discrepancies in steep velocity-gradient regions. The small discrepancies found in this experiment give rise to a limitation of the PIV technique. If the flow field in question contains regions of both high and low velocity, an image separation time which gives a reasonable particle displacement for the low-velocity region may be too short to measure any appreciable displacement in the high-velocity region. Conversely, a separation time which is reasonable for the high-velocity region, may be too long for the low-velocity region, and consequently some movements of the particle may be missed during the separation time. An intermediate separation time must be chosen which will accommodate velocity measurement in both regions.

PIV has also proven to be a viable technique for determining velocity fields in aerodynamic applications. Characteristics of flow around a 1 mm diameter smooth brass cylinder were investigated by Grant and Smith [9]. A high-powered, Q-switched Ruby laser was used, with its available 10 J distributed between 2, 3 or 4 pulses each of length 25 ns. Its beam was shaped into a sheet by a convex cylindrical lens followed by a concave spherical lens. An air flow of 3.4 m/s was used in the experiments giving a Reynolds number of 207. This flow was seeded with oil droplets from an aerosol generator with diameters in the range of 1 - 5 μm , and images of the droplets were recorded by a 35 mm camera on Kodak Technical Pan 2415 film. Young's fringe analysis was performed, however the processing algorithm used to determine

velocity fields was not described in the paper. Other aerodynamic PIV applications performed by the above authors include vortex shedding from cylinder pairs, vortex shedding from structural elements with special attention to separation, flow around model offshore platforms and flow over an inclined plate.

Grant and Smith [9] also applied the PIV technique in the area of hydraulics, specifically to the study of wave motion. Waves generated by a programmable flap system were seeded with aluminum particles whose diameter were in the range of 20-50 μm . A mechanical chopper was used to pulse the beam of a 18 W continuous wave Argon-ion laser, which was then shaped into a light sheet and guided into the test section producing an illuminated cross-section of the wave. Excellent correspondence between experiment and theory was found. The unsteady nature of a wave's motion makes PIV an ideal tool for determining its velocity field, as measurement of the entire wave takes place instantaneously. Also, PIV allows the wave to be captured at the critical moment (breaking). This is important since no one breaker is identical to another, and consequently there exists a real need for velocimetry studies on breakers.

The characteristics of flow behind a rearward facing step have been investigated extensively in the past, using LDA and numerical methods. Grant et al. [17] applied the PIV technique to this situation using an 18 W cw Argon-ion laser chopped by a rotating disk with a transparent segment, and shaped into a fan of approximately 2 mm thickness by a glass rod. Multiple images of neutrally buoyant particles with a mean diameter of 60 μm were recorded by a still camera on high resolution film. The film was then illuminated with a uniform white light and examined by a video camera whose output was digitized and held by a frame-store in an array of 256 x 256 pixels. The digitized image was then reduced using algorithms which directly identified the particle images and used a multi-stage pattern recognition procedure to obtain velocity and turbulence estimates. Velocity and turbulence fields corresponded fairly well with

LDA measurements. Variations between the results of the two techniques were attributed to measurement errors involved in both techniques, and the statistical uncertainty caused by the limited number of PIV samples.

A rather unique application of PIV was performed by Wozniak and Wozniak [18], in which thermocapillary convection was investigated. The test cell consisted of a rectangular cavity with horizontal copper endwalls. At each endwall a constant, but different uniform temperature was maintained. To establish a vertical temperature gradient within the liquid, the upper wall was heated via an electrical resistance heater and the lower wall was cooled with a constant temperature coolant by a common thermostatically controlled circulator. The upper wall contained a bore hole in its centre, to inject air into the test cell which was filled with silicon oil, seeded with neutrally buoyant 5 μm polystyrene spheres. Sheet illumination was provided by a 2 W Argon-ion laser, and images were recorded by a still camera on Kodak Technical Pan Negative. An experiment consisted of heating the liquid from above and cooling it from below until a steady temperature profile between the horizontal plates was established, then injecting an air bubble and photographing the steady convection flow once it developed. The photographic negative was then interrogated by an unexpanded laser beam and the resulting Young's fringes were imaged by a CCD video camera and digitized by a frame grabber board integrated into a personal computer. The FFT method was used to determine fringe spacing and orientation. The results of their experiments showed the velocity distribution caused by the thermocapillary flow. They found that there existed primary and secondary vortices which moved toward the pole of the bubble with increasing temperature gradients. The shape of these vortices resulted from the interaction of surface tension and buoyancy forces. The relatively high flow velocities near the contour of the bubble indicated that the surface 'drives' the flow. This example demonstrates that PIV is a useful tool for full-field convective flow analysis. In particular, for thermocapillary

flows where the magnitude of the velocities is relatively low, PIV provided satisfying results.

2.3.2 Three-dimensional Applications

Three-dimensional PIV is usually applied to complex flow conditions where the third (out-of-plane) velocity component plays an important role in the flow field. Normally, the third component is inferred from several parallel velocity fields by numerical processing.

A 3-D aerodynamic application of PIV was performed by Towers et al. [19] in which the transonic flow around a model aircraft wing was investigated. Experiments were performed on a 1/20 scale, half-span, vertically oriented model of a civil aircraft with a turbine powered engine simulator (TPS). The TPS produced a central core jet surrounded by a by-pass jet. The exit pressures of the two flows modelled the real flow from a high-bypass turbofan engine, which is fully three-dimensional and highly turbulent. A frequency-doubled Nd:Yag laser, Q-switched to give a pulse duration of 10 ns, was used to form the light sheet, and a galvanometer rotated the horizontal light sheet vertically so that different planes could be scanned. An array of 16 aerosol generators, placed 9 m upstream of the model, was used to seed the flow. Images of particle pairs were recorded by a CCD camera for flow speeds from 0.2 to 0.8 Mach number. The seeding particle density was found to be 3 particle pairs per cm^2 at a Mach number of 0.2. This decreased to 0.5 particle pairs per cm^2 at 0.8 Mach number. A three-dimensional volume of the flow was investigated by imaging particles on many adjacent planes, accomplished by moving the light sheet vertically in small increments and refocusing the camera at each position. Each plane was then analysed using a spatial domain algorithm to identify particle pairs and calculate particle velocities. It was estimated that velocity measurements at 0.8 Mach number could be made to within 4 %. A problem encountered in this analysis was the high operational costs of the wind tunnel - \$40,000 per day. This makes PIV ideal for this situation, as data can be accumulated

faster than with other laser diagnostic methods such as LDA.

Chen et al. [7] performed a three-dimensional PIV analysis on the flow in a cubic chamber, with offset inlet and outlet ducts. Although the geometry of the chamber was simple, various complex flow patterns were generated and analysed. A two-dimensional light sheet was created by shaping the beam of a 2 W ion laser with two rectangular cylindrical lenses. To scatter the laser light, the working fluid (water) was seeded with Pliolite particles, 50 μm or less in diameter. An inlet flow velocity of 0.015 m/s was used, which gave a Reynolds number of 298 based on the inlet height and inlet velocity. The light sheet was used to slice the internal three-dimensional flow into 6 two-dimensional flow images at prescribed locations, three in the axial direction, and the other three perpendicular to the axial direction. Particle images were recorded by a CCD camera, and digitized by a frame grabber board on a personal computer. The images were then analysed using the cross-correlation technique (see section 2.2.4.2), and the resulting six full-field velocity profiles allowed the three-dimensional flow in the cubic chamber to be inferred. Flow patterns such as stagnation points, three-dimensional separation, recirculation and vortex formation were observed in the chamber. These features were then used to verify the numerical simulation performed in the same study, however the measured data was not accurate enough for verifying velocity profiles at any selected location.

Arroyo et al [11] performed a three-dimensional study of Rayleigh-Bénard convective flow in a small box. Rayleigh-Bénard [20] convection takes place in a fluid contained between two horizontal plates and subjected to an adverse vertical temperature gradient. The flow is determined by the physical properties of the plates, the geometry of the cell, and the physical properties of the working fluid. In this case, the cell was rectangular and the temperature difference between the two horizontal plates was maintained (within 0.01 °C) by water circulating in contact with the plates from two independent thermostatic baths. The cell was filled with

silicone oil and seeded with latex particles having diameters ranging from 1 to 20 μm . Sheet illumination was provided by a 5 mW He-Ne laser expanded with a microscope objective and focused with a cylindrical lens. The position of this illuminating sheet relative to the flow was controlled by a mechanical stage on which the cell was mounted. An electromechanical chopper pulsed the light sheet to create multiple exposures of each particle, using pulses of width 120 ms and separations ranging from 1.4 s (in the midplane) up to 5 s (near the walls). About ten exposures were taken in each photograph by a Nikon FM2 still camera, on Kodak Technical Pan 2415 film. Young's fringe analysis was used to determine the two in-plane velocity components for each particle, from the resulting multiple exposure photographs. The overall uncertainty associated with the measurement of the velocity vectors was estimated to be 1 % of the full-scale velocity. Other two-dimensional information such as flow rate, vorticity and streamlines were obtained by numerical processing of the two-dimensional velocity field. The third (out-of-plane) velocity component was found by applying PIV to 15 parallel, symmetrically and regularly spaced, planes of the flow, and then calculating the third component from the resulting velocity fields. The procedure, based on the continuity equation, found the maximum out-of-plane velocity component to be 35 $\mu\text{m/s}$, which was small, but still significant as compared to the two in-plane velocity components which ranged from 150 $\mu\text{m/s}$ to 200 $\mu\text{m/s}$. Using numerical processing similar to the two-dimensional analysis, three-dimensional flow information was plotted such as streamlines, vorticity and flow rate. The extensive information obtained in this work allowed the authors to conclude that the flow pattern was essentially three-dimensional throughout the entire flow field.

Arroyo and Greated [21] combined PIV and stereoscopy to measure the three-dimensional velocity field in an acoustic streaming flow. In stereoscopic PIV, the flow is viewed from two different positions, and two pictures of the flow are taken simultaneously by the same camera,

using a system of mirrors. The fact that each recorded image will be different, is then used to calculate the magnitude of the out-of-plane component. The accuracy of the out-of-plane component increases with the distance between the two viewing directions. To demonstrate the applicability of stereoscopic PIV, the technique was applied to acoustic streaming, which is the generation of non-zero motion by a sound field. Streaming was produced by introducing sound of frequency 1910 Hz into a rectangular tube using a horn loudspeaker with the horn removed. Light from a 4 W argon laser, optically shaped into a light sheet of thickness 0.7 mm, was transmitted through the tube, where smoke had been introduced to render the flow visible. An electromechanical shutter was set to produce pulses of duration 30 ms with a separation of 300 ms. The mirror system was positioned so as to displace the two images along the tube axis. Photographs were taken by a still camera and the resulting images were analysed using Young's fringe analysis. Good correlation was found when experimental results were compared to theoretical calculations. It was noted that the out-of-plane velocity measurements exhibited more random deviations from the theoretical values than the in-plane measurements, corresponding to a smaller accuracy in that component. The error in the out-of-plane component was estimated to be about three times greater than that of the in-plane components, which is the same as in the 2-D PIV system. Stereoscopic PIV has its advantages in that it allows the three velocity components to be obtained simultaneously, and since it is quite similar to conventional PIV, its implementation is very straight-forward.

Kasagi and Nishino [22] with their colleagues at the University of Tokyo, developed a three-dimensional particle-tracking velocimeter which was characterized by the use of three TV cameras, sophisticated camera calibration and highly automated data reduction and analysis. Applications of this 3-D PTV undertaken at the University of Tokyo include unsteady laminar Couette flow between two concentric cylinders [23], nearly isotropic decaying turbulence [24,25],

fully developed 2-D turbulent channel flow [26], an axisymmetric free jet [27], separated flow downstream of a 2-D abrupt expansion, [28,29] and turbulence near a free surface [30]. In each case, the measurement volume was illuminated by a stroboscope with a flash duration of 20 μs . The flashes were triggered at 60 Hz at the beginnings of alternate scans of the odd and even TV fields that constitute one TV frame. Consequently, two consecutive images of the nylon 12 particles (diameter $\approx 200 \mu\text{m}$) used to seed the flow, were obtained at an interval of 1/60 s, and such an image pair was recorded at an interval of 1/10 s. The first step in data reduction was to determine camera parameters such as position, orientation and focal length of the camera. This was performed by (1) taking images of calibration points printed on a calibration mechanism and (2) numerically solving the perspective equations which relate absolute and image coordinates of the calibration points in terms of the camera parameters. Next the centroid of each particle image was calculated as a gravitational centre of pixels. Using these centroids along with the camera parameters, the particle velocities were determined by: (1) calculation of three-dimensional particle positions, (2) particle tracking over 1/60 s, and (3) vector tracking over 1/10 s. In general it was found that the 3-D PTV could be a very powerful tool for measuring various turbulent flows. However, the number of instantaneous vectors obtained still remains too small to fully resolve turbulence structures of interest, and further work in this area is needed.

2.3.3 Summary

A number of conclusions can be drawn from previous research as to the applicability and accuracy of PIV. It appears that the PIV technique can be applied to almost any flow condition whether it be laminar or turbulent, two-dimensional or three-dimensional, involving low or high velocities. To evaluate the applicability of PIV, a comparison will be made to LDA. Like LDA, PIV is non-intrusive and therefore does not disturb the flow. The two techniques may be

considered complimentary in the sense that LDA measures a velocity-time record at a single point in space whereas PIV measures a spatial record at a single point in time [5]. The PIV system is much less efficient than the LDA system in obtaining basic velocity information, however it is difficult to apply the great efficiency of LDA in capturing data to the measurement of spatial structures. Thus, PIV systems have an important niche to fill, where spatial structures are the primary goal of a measurement [5]. Data acquisition for LDA is very time consuming and requires the existence of steady state conditions. PIV has the ability to investigate unsteady flow regimes as it provides instantaneous velocity vectors. Data acquisition time for PIV is far less than for LDA, since the former obtains an instantaneous measurement of the entire flow field and the latter obtains measurements point-by-point. Thus, PIV is ideal for situations where facility run time is costly. Although PIV data acquisition is relatively fast, subsequent data analysis is rather time consuming. With the advent of more powerful computers and efficient software, it is expected that this problem will soon be eliminated.

A major drawback to the PIV technique is that in order to obtain accurate velocity measurements, an elaborate experimental system is required, which is difficult and costly to construct and operate. The requirement of a very powerful light source, normally a pulsed Ruby or Nd:Yag laser, contributes substantially to the high cost of the system. Image processing is also a major contributor to this cost, requiring sophisticated software and powerful hardware.

2.4 Mixed Convection in Enclosures

From the above examples it would appear that the application of PIV to a mixed convective flow in an enclosure is feasible and worthy of investigation. This section discusses some mixed convective flow theory and presents the current problem specification.

Convective heat transfer is defined as the transfer of heat to a fluid in motion. Natural

or free convection and forced convection are the two distinct modes of convective heat transfer. The rate of heat transfer is estimated by considering one of these modes to be dominant. However, in any situation involving heat transfer, temperature differences exist in the boundary region near a heated or cooled surface. This results in density gradients in the ambient medium, and in the presence of a body force such as gravity, natural convection effects arise. Thus, in any forced convection circumstance, natural convection effects are also likely to be present [31]. It becomes important to determine how large these buoyancy effects are as compared to the forced convection effects, and under what conditions they may be neglected. Conversely, if the buoyancy effects are of greater relative magnitude, the question is whether the forced component of convection can be neglected. In many cases, both natural and forced convection effects are significant, and this is referred to as mixed or combined convection. A parameter which characterizes mixed convection is the Richardson number given by:

$$Ri = \frac{Gr}{Re^n} \quad (2.24)$$

where the Grashof number, Gr and the Reynolds number Re , represent the vigor of the natural convection and forced flow effects, respectively. The exponent n , depends on the geometry, the thermal boundary conditions, the fluid, etc. Free convection is considered negligible if $Ri \ll 1$ and forced convection is negligible if $Ri \gg 1$. Therefore, the combined or mixed convection regime is one for which $Ri \approx 1$ [32].

The effect of buoyancy on heat transfer in a forced flow is strongly influenced by the direction of the buoyancy force relative to that of the flow [32]. When the buoyancy force and the forced motion are in the same direction, buoyancy effects enhance the rate of heat transfer associated with pure forced convection, and the flow is said to be "aiding flow". When they are in opposite directions, the flow is said to be "opposing flow", since buoyancy acts to decrease

the rate of heat transfer. It should be noted that although buoyancy effects can significantly enhance heat transfer for laminar forced convection flows, enhancement is typically negligible if the forced flow is turbulent [32].

Figure 2.5 shows a schematic diagram of the rectangular enclosure used by Nurnberg [2], and in the present study to investigate flows involving mixed convection. A horizontal inlet jet, with specified velocity and temperature profiles (u_i and T_i respectively), enters the cavity at the upper left corner. The fluid exits the cavity through a horizontal duct at the lower left corner of the cavity. All solid boundaries are insulated, with the exception of the right vertical wall which is maintained at a uniform temperature, T_w .

Dimensionless parameters can be used to specify the flow conditions. The first is the fluid Prandtl number, defined as the ratio of momentum to thermal diffusion, given by:

$$Pr = \frac{\mu_f C_p}{K} = \frac{\nu_L}{\alpha_L} \quad (2.25)$$

where μ_L is the dynamic viscosity of the fluid, C_p is the specific heat at constant pressure, K is the thermal conductivity of the fluid, ν_L is the kinematic viscosity, and α_L is the thermal diffusivity of the fluid. The inlet ratio, a is defined as the ratio of the inlet height to the cavity height, expressed as:

$$a = \frac{D}{H} \quad (2.26)$$

The ratio of the height to width of the cavity, called the cavity aspect ratio, A is given by:

$$A = \frac{H}{W} \quad (2.27)$$

The inlet Reynolds number Re , is the ratio of inertial to viscous forces, defined as:

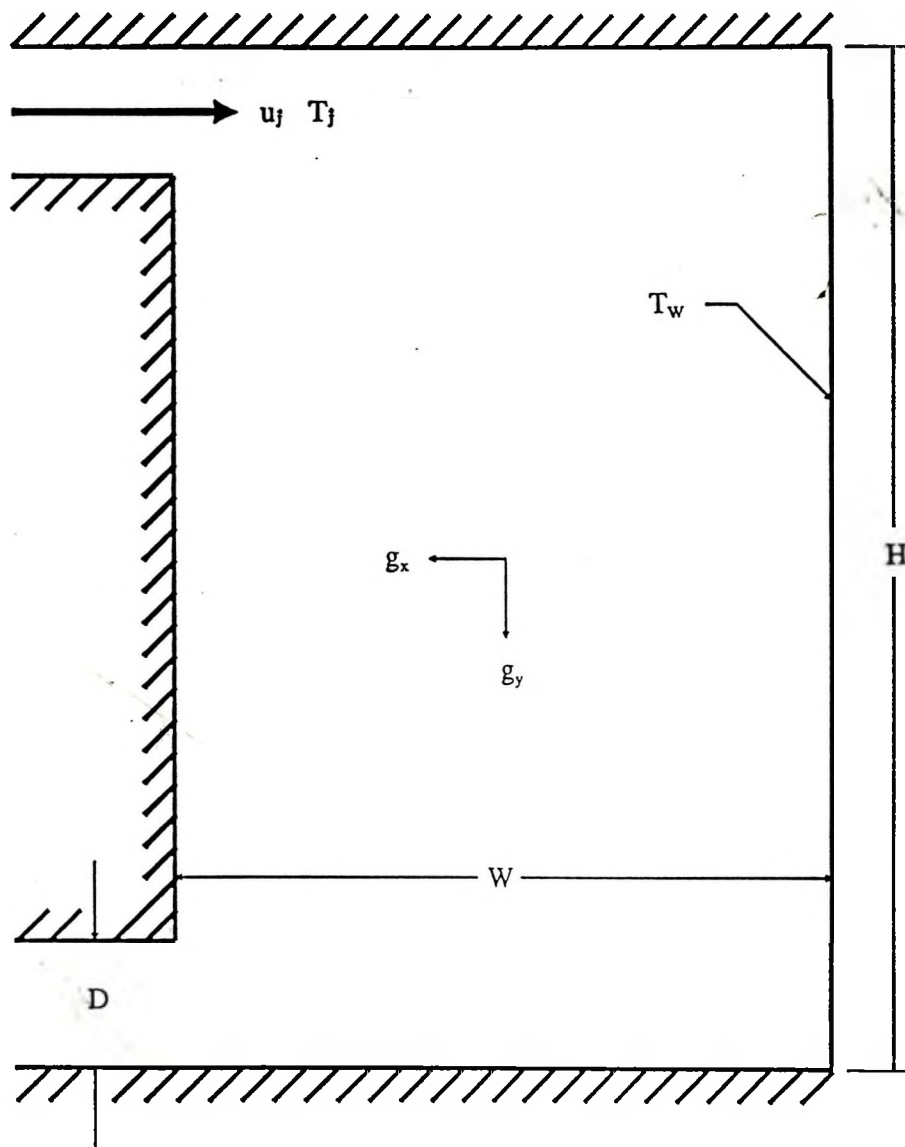


Figure 2.5 - Problem Specification [2]

$$Re_D = \frac{uD}{\nu_L} \quad (2.28)$$

The system Grashof number, relates the buoyant to viscous forces and is given by:

$$(Gr)_L = \frac{g\beta(T_w - T_f)L^3}{\nu_L^2} \quad (2.29)$$

The subscript i refers to component of gravity and the subscript L refers to the length scale. In this situation, the component of gravity acting on the fluid is g_y . The length scale is chosen as the height of the cavity, H as a boundary layer forms on this vertical surface.

In Figure 2.5, the inertia of the fluid jet entering at the top left corner of the cavity drives the fluid across the top boundary. Continuity first turns the fluid vertically to flow down the right boundary and again to flow horizontally along the bottom boundary toward the outlet of the cavity. As the fluid flows past the right boundary, heat transfer takes place. If the temperature of the wall is less than that of the fluid, heat is transferred to the wall and a downward buoyancy force is created. Since buoyancy and inertial forces are acting in the same direction, the flow is said to be "aiding flow". Conversely, if the temperature of the wall is greater than that of the flowing fluid, heat is transferred to the fluid resulting in an upward buoyancy force. Since buoyancy and inertial forces are acting in opposite directions, the flow is said to be "opposing flow". The aiding or opposing nature of the flow may be characterized by the Grashof number [2].

$Gr_L > 0$	opposing flow
$Gr_L = 0$	isothermal flow
$Gr_L < 0$	aiding flow

Since mixed convective flows involve both inertial and buoyancy forces, the resulting nature of the flow is largely dependent on the Richardson number, which is the ratio of buoyant to inertial forces. Physically, the magnitude of the Richardson number indicates the relative

effect of buoyancy on forced convection [31]. For the flow conditions specified above, the value of the exponent n in the equation for the Richardson number (eq. 2.24) is 2 [31].

Nurnberg [2] and the present work investigate the case of opposing flow, as opposing effects have not been considered in comparable detail to aiding flow regimes, and there is little information on possible flow separation and reversal [31].

CHAPTER 3

EXPERIMENTAL SYSTEM

3.1 Experimental Apparatus

The following sections describe the experimental apparatus used in the present application of PIV. A schematic diagram of the PIV system is shown in Figure 3.1.

3.1.1 Test Cavity and Flow Loop

The test cavity and flow loop used in the present experiments was constructed by Nurnberg [2] for use in similar experiments in which he used LDA to verify his numerical code. The cavity, shown in Figure 3.2, is constructed from 25.4 mm-thick clear acrylic and has a height of 297 mm, a width of 149 mm, and a depth of 48.5 mm. A horizontal jet of width 8 mm ($D_H = 13.7$ mm) enters the cavity at the top of one vertical wall. A 203 mm development length allows the flow to become fully developed before entering the cavity. The entrance to this development length measures 12.7 by 12.7 mm ($D_H = 12.7$ mm). The flow exits the cavity at the bottom of the same vertical wall through an exit channel which is geometrically similar to the entrance.

The opposite vertical wall is constructed from a 9.5 mm thick copper plate and is maintained at a uniform temperature by 10 independently controlled, electric film heaters placed on the back of the copper plate. Eighteen iron/constantan thermocouples located at approximately 0.5 mm from the inner surface, are used to measure the inner wall temperature. Ten of these thermocouples are located on the centre line of the copper wall and

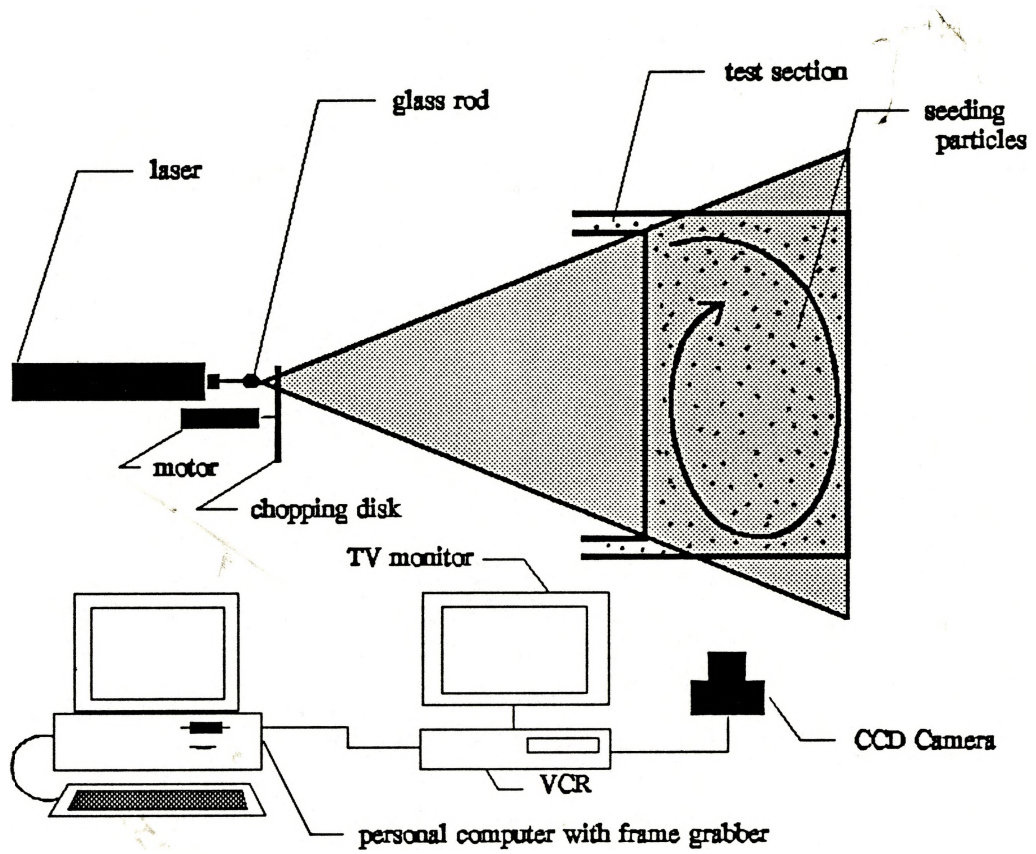
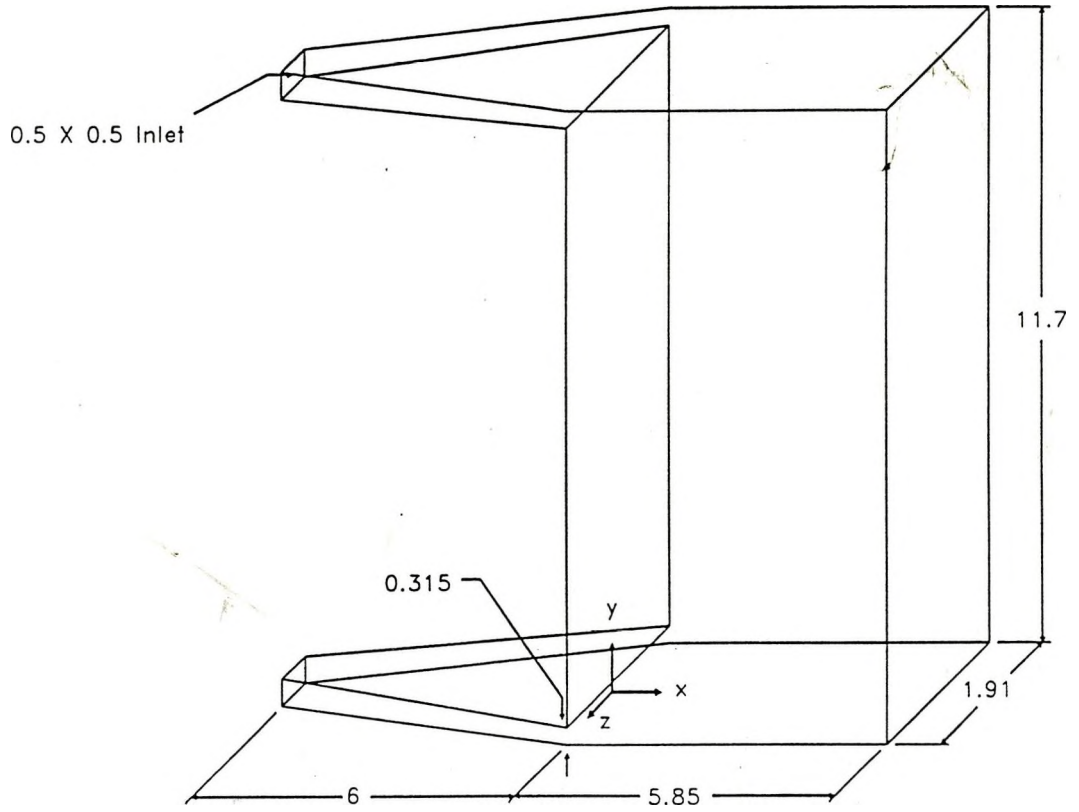


Figure 3.1 - PIV System Schematic Diagram



Note: All dimensions in inches

Figure 3.2 - Experimental Test Cavity [2]

the remaining eight are offset to ensure a uniform two-dimensional temperature distribution. A chromel/alumel thermocouple probe is placed in the flow at the entrance to the development length to measure the average inlet temperature of the working fluid, T_1 . The outlet temperature, T_2 , is measured by a similar probe placed at the exit of the outlet development length.

The test cavity is placed in the flow loop as shown in Figure 3.3. The working fluid, (water) flows from the head tank to the inlet of a centrifugal pump (Little Giant model 3E-12NRT). The outlet of the pump is connected to a flow control valve which regulates the flowrate through the system. The water may then flow into the test cavity passing through a flowmeter (Brooks Rotameter A-8M-25-4), or it may flow in a bypass loop back to the pump inlet. As the water flows into the test cavity, it is heated by the electric film heaters. After exiting the cavity the water flows through a counterflow heat exchanger where it is cooled, and then returns to the head tank. Coolant water for the heat exchanger is provided by cold tap water and is controlled by a control valve.

3.1.2 Light Source and Optics

The light source used for the experiments is a 15 mW Helium Neon laser, Spectra-Physics Model 120, emitting light at a wavelength of 632.8 nm. A 9.5 mm diameter glass rod focuses the output beam of the laser (initial diameter = 0.67 mm) into a two-dimensional fan approximately 1 mm thick. To pulse the laser light, a mechanical chopping disk shown in Figure 3.4, was manufactured according to results found in preliminary investigations.(see Section 3.2.2 and Appendix A) This disk is rotated by a small DC motor made by Electrocraft which is connected to a power supply (Anatec Electronics Ltd. model 50-1S). A motor support was also manufactured, which positions the motor at a height where the laser beam

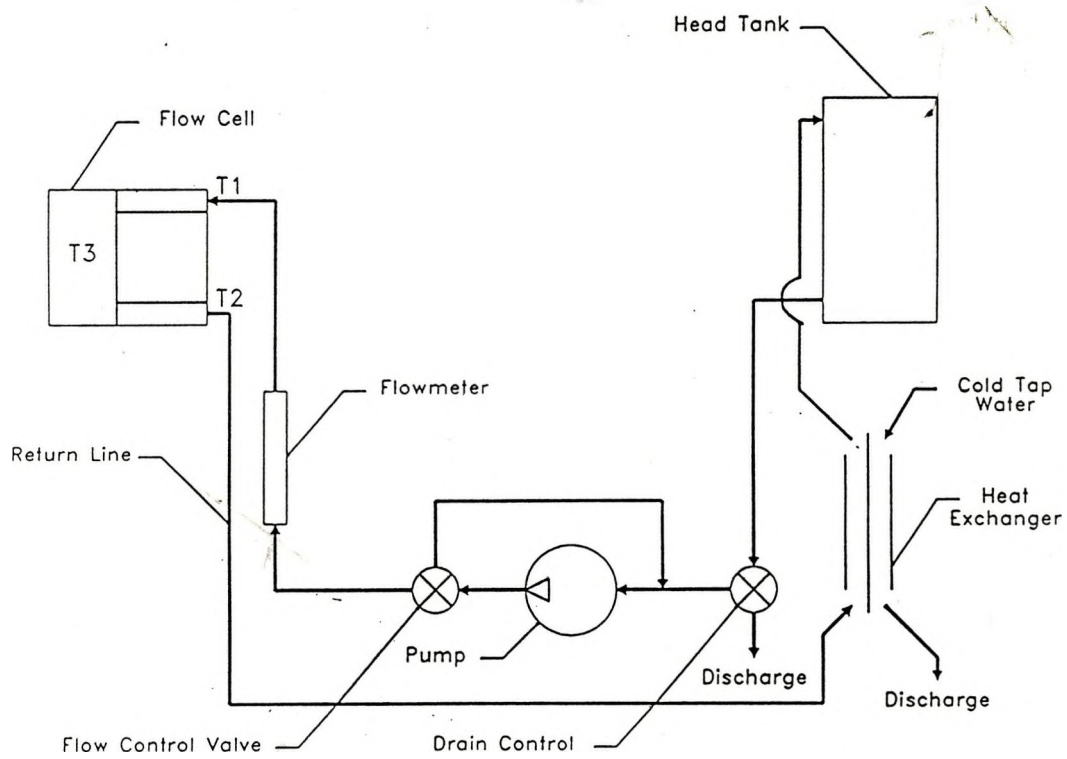


Figure 3.3 - Experimental Flow Loop [2]

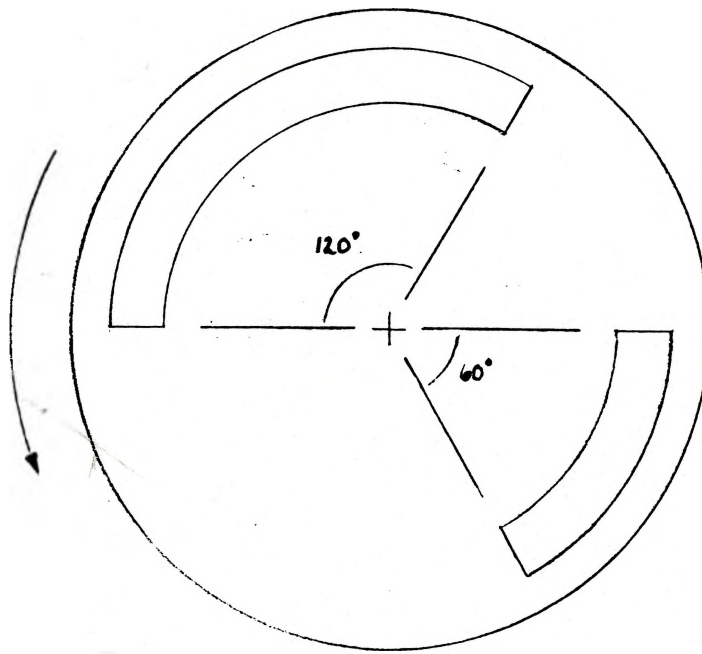


Figure 3.4 - Mechanical Chopping Disk

passes through the slots in the chopping disk. This support was designed to minimize any vibration from the motor to the table on which the experimental apparatus is placed. A hand-held digital tachometer (photo type) manufactured by K.B. Electronics measures the number of revolutions per minute of the disk, which is needed to calculate the total exposure time of the two particle traces. The accuracy of the tachometer measurement is within ± 1 RPM, which translates to an error of $\pm 2.78 \times 10^{-5}$ seconds in the calculation of the total exposure time. This error is considered to be negligible in calculating the accuracy of the velocity measurement.

As shown in Figure 3.1, the sheet of laser light is directed through the test cavity, so that it illuminates a plane of the flow perpendicular to the heated wall. The construction of the test cavity prohibits the investigation of planes which are parallel to the heated wall.

3.1.3 Light Scattering Medium

Polystyrene particles ($\rho_p = 1.03 \text{ g/cm}^3$) with diameters ranging from 105 to 125 μm are used to scatter the laser light as they enter the light sheet. With a density close to that of the working fluid, it is assumed that the particles follow the flow accurately as they are neutrally buoyant. Nurnberg [2] determined that particles of this diameter follow the turbulent fluctuations experienced in these experiments. He calculated the particle time scale as recommended by Buchhave et al. [33]:

$$\tau_p = \frac{d_p^2}{36\nu_L} \left[2 \frac{\rho_p}{\rho_L} + 1 \right] \quad (3.1)$$

where d_p is the diameter of the particle, ν_L is the kinematic viscosity of the fluid and ρ_p and ρ_L are the densities of the particle and fluid respectively. For particles of diameter between 105 μm to 125 μm , and a density of 1.03 kg/m^3 , the time scale was within the Kolmogorov

requirement, which estimates the time scale of the turbulent fluctuations by:

$$\tau_k = \left[\frac{\nu}{\varepsilon} \right]^{1/2} \quad (3.2)$$

where ε is the dissipation of turbulent kinetic energy.

The slip velocity for a particle of this size, calculated by Stokes Law (eq. 2.1) is 1.002×10^{-4} m/s, which is considered to be very small as compared to the particle velocities encountered in the experiments. This indicates that this size of particle follows the flow accurately. For this calculation, an estimate of particle acceleration was made using Nurnberg's [2] velocity results near the separation point. It can then be assumed that if a particle can follow the flow accurately in this highly turbulent region, it will perform similarly in the remainder of the flow. From Nurnberg's [2] results, in the region of separation, velocity differences of 0.0252 m/s occurred over a 0.005 m length-scale, corresponding to a particle acceleration of 0.127 m/s^2 . The calculated slip velocity is then 0.4 % of the velocity difference, and 0.2 % of the full-scale velocity.

This particle size was chosen for the above reasons as well as its suitability to the resolution of the present imaging equipment. It was found that the lower resolution limit of the CCD camera being used was $89 \mu\text{m}$, and therefore no optical advantage could be realized by imaging particles smaller than this value.

The particles are introduced into the flow loop by placing them in the head tank. Since the water flows through a closed loop, once an appropriate particle concentration is found by trial and error, it can be maintained throughout the experiments. An appropriate particle concentration is considered to be one that is sufficiently dense to accurately resolve all regions and length scales of the flow field, and yield a high data density. However, this concentration must also be sufficiently low enough to record individual particle images, rather

than speckle patterns.

Although the particles are neutrally buoyant, the water in the head tank is periodically agitated so that particles do not settle, which ensures a more uniform particle distribution.

3.1.4 Recording Medium

A black and white CCD camera (Panasonic model GP-MF552) connected to a Super VHS VCR (Panasonic AG-1830) was used to capture particle images on video tape. A CCD imager is a metal-oxide-semiconductor (MOS) that is composed of a two-dimensional array of closely spaced independent sites (pixels) where photon-induced charge is stored. When the pixels are exposed to light, a charge pattern accumulates corresponding to the intensity distribution of the object that is being imaged. Depending on the CCD used, the physical distance between pixel centres ranges from 6 to 30 μm , and each pixel is usually square. The camera used in the present work is equipped with a 2/3 " ITL image sensor with an array of 768 (H) x 493 (V) pixels, with each pixel measuring approximately 11.5 (H) x 13.4 (V) μm . A 50 mm lens, assumed to be aberration free, focuses the incident light onto this sensor. Operation of the CCD is based on the photoelectric effect; photons incident on the chip cause electrons to be emitted and collected into an image area called the parallel register. Electrodes in the parallel register act as gates when properly biased with electric potential, establishing potential wells, where the accumulated electrons are stored. The amount of electric charge stored is proportional to the incoming light intensity and the time of exposure. A programmed sequence of changing gate potentials propagates the potential wells across the CCD chip moving the charge one pixel row at a time to a serial register where the charge in each pixel is individually shifted toward an output amplifier. The output amplifier produces an amplified and measurable signal that is proportional to the charge in each pixel, creating an

image on a monitor connected to the camera. With an excellent spectral response of 85 % at 632.8 nm, this camera is ideal for use in the present experiment. The VCR was used to record particle movement on Super VHS video tape for subsequent image analysis. This video tape was used as its high resolution provides images of better quality than standard video tape.

Results found in the preliminary investigations (see Section 3.2.2) indicated that in order for images of sufficient quality to be produced, small sections of the flow must be imaged and analysed separately, and then combined to obtain the entire velocity field. A 1-cm uniformly-spaced grid was placed on the back of the test section to locate and record particle movements in each of the 24 sections measuring 4 cm x 5 cm. Since the grid was recorded along with the particle traces, it was also used to spatially calibrate their movements during image analysis, i.e. to find the system magnification.

3.1.5 Image Analysis

Image analysis was performed manually with the use of a personal computer (486 MHz) equipped with a frame grabber board, model DT2853 from Data Translation, and a measurement software package called SigmaImage/Scan written by Jandel Inc. This software package enables the user to view individual video frames, change the contrast, and spatially calibrate so that measurements can be performed. For each 4 cm x 5 cm section, the frame grabber was used to "grab" thirty frames from the video tape. Each frame was individually loaded into SigmaImage/Scan, its contrast enhanced so that particle traces were visible, and spatially calibrated using the grid imaged along with the particle motion. An image of one centimetre contained 108 pixels, corresponding to a system magnification of 3.75. This is calculated from the ratio of the number of pixels in the image of one centimetre to the number

of pixels in one centimetre of the computer screen. This magnification is different from that used in the equations in Chapter 2, which is the magnification of the recording system. This intermediate magnification from the test cavity to the CCD chip was found to be 0.1242, which is the ratio of the number of pixels in the image of one centimetre to the number of pixels per centimetre of the CCD chip. Each frame was scanned for acceptable particle traces and measurement of particle displacement was performed by "clicking" the mouse on the beginning and end points of a particle trace. SigmaImage/Scan recorded the x and y position of these points in a spreadsheet file for each section. For each of the three cases investigated, 30 frames from each of the 21 sections of the test cavity were examined, giving a total of 1890 video frames examined to obtain velocity data.

3.1.6 Data Manipulation

The data contained in the SigmaImage/Scan spreadsheet files was used to calculate the u and v components of the vectors comprising the entire velocity field. The horizontal velocity component, u, was determined by calculating the magnitude of the particles' displacement in the x direction and dividing it by the total exposure time (calculated in Appendix A). The vertical velocity component (v) was similarly determined. TECPLOT Version 4.0 written by Amtec Engineering was used to create plots of the velocity vectors, however this software requires that the velocity information be provided on a regularly spaced grid. A FORTRAN program was written to average the random velocity vectors onto two different grids which are shown in Figure 4.2 (a) and (b). From the list of random u and v components comprising the entire velocity field, the program divided the field into 1 cm x 1 cm (Grid 1) or 0.5 cm x 0.5 cm (Grid 2) interrogation areas, searched each area for values, totalled each component separately, and divided each total by the number of values found for

each component. This was performed for the entire velocity field and the resulting average vector tails were placed at the centre of the corresponding interrogation area. If no values were found in the interrogation area, the velocity was set to zero. The velocity fields for each of the three cases are presented and discussed in the next chapter.

3.2 Experimental Procedure

3.2.1 Preparation of Test Cavity

According to Nurnberg [2], approximately three to four hours is required for flow conditions to reach steady state. The instantaneous nature of the PIV technique does not demand this. However since the entire velocity field is not imaged instantaneously, steady state conditions must exist. To verify the work done by Nurnberg [2], an attempt was made to duplicate the same conditions he investigated. Table 3.1 gives relevant information for each of the three cases performed in the present work. The following experimental procedure was followed for Cases 2 and 3. In Case 1, the wall was not heated and only steps (1), (2) and (9) were followed. Refer to Figure 3.3 for a diagram of the flow loop.

- (1) Turn on the cold tap water to the heat exchanger. Allow warm water in the building's piping system to purge.
- (2) Turn on the pump and adjust the flow control valve to the desired flowrate.
- (3) Turn on the wall heaters and coarsely adjust the electrical input. Allow the system to stabilize for approximately 15 minutes.
- (4) Repeat step 3 until the wall temperatures are near the required temperatures.
- (5) Adjust the cold water flowrate to the heat exchanger to obtain the required inlet temperature (T_1).
- (6) Finely adjust the power to each of the heaters until the required wall temperature

is achieved. The wall temperature is considered to be uniform when the temperature difference between maximum and minimum measured temperatures is less than 1.0°C.

- (7) Finely adjust the flow control valve to the required flowrate.
- (8) Go to step 5 until the required temperature and velocity requirements are obtained.
- (9) Allow the system to stabilize for approximately three hours.

Table 3.1 - Experimental Data

CASE	1	2	3
u_j (m/s)	0.0887	0.0887	0.0377
T_w (°C)	20.7	50.67	80.98
T_1 (°C)	20.7	22.4	27.2
N_{chopper} (RPM)	1150	1150	1150

3.2.2 Preliminary Investigations

Before actual PIV measurements were obtained, preliminary investigations were performed to acquire qualitative information about the flow and quantitative information to design the light chopping disk. Velocity conditions similar to those expected in the main experiments were established, however in order to save time and energy, the wall was not heated for the preliminary investigations. The light sheet, created as in section 3.1.2, was used to illuminate an arbitrary plane of the flow within the test cell. With the room darkened, photographs were taken with a Canon AE-1 35 mm camera equipped with a 50 mm lens. In the first experiment, Kodak 100 ASA colour film was used, with exposure times varying from

1/8 to 2 seconds in duration, an $f/No.$ of either 1.8 or 22, and a flowrate of 54 % or 93 % of the maximum flowrate the pump could deliver. Various combinations of exposure time, $f/No.$ and flowrate were investigated. Having such low sensitivity, this film did not sense any light for exposure times under 1/2 second, and exposure times longer than this produced particle streaks. It was also found that in these low light conditions, the smallest $f/No.$ possible must be used. With this knowledge, a second experiment was performed using highly sensitive Kodak p3200 ASA film. Again, photographs were taken using combinations of exposure times and flowrate, but in this instance a constant $f/No.$ of 1.8 was used. For flowrates of 50 %, 64 % and 90 % of the maximum flowrate, relatively clear particle images were obtained with an exposure time of 1/30 of a second. Below this value, the film did not sense any light, and above this value particle streaks were obtained. Specific details of these experiments, such as the exposure time/flowrate combinations investigated, can be found in Appendix A.

With the information obtained in these preliminary investigations, as well as knowledge of the high sensitivity of the CCD camera and velocity information from Nurnberg [2], a mechanical light chopping disk was manufactured. As can be seen in Figure 3.4, the disk contains two slots which allow the laser light to reach the test section, for short periods of time. The combination of the length of the slot and the speed of rotation of the disk determines the exposure time. Since the CCD camera is far more sensitive than photographic film, and the velocities encountered in the mixed convection experiments are smaller than those investigated here, the slots were made shorter than originally expected. It was also decided that the disk would be rotated at a sufficiently low speed to produce particles streaks rather than particle images. This was necessary to determine the particle direction using manual image analysis. In order to determine the direction of the particle, one slot was made

slightly longer than the other. From the location of the longer trace relative to the shorter trace, the direction in which the particle was displaced within the total exposure time can be determined. The total exposure time is calculated from the beginning of one slot to the end of the other. Measuring the displacement of the particle from the beginning of the first trace to the end of the second, and dividing this value by the total exposure time yields the velocity magnitude of the particle. Subsequent trial experiments were performed using the light chopper and the CCD camera to record particle motion on video tape. With the light sheet illuminating the entire flow field, it was found that the light emitted from the laser was not sufficient to produce measurable particle image traces. Therefore, it was decided to illuminate smaller segments of the flow field, moving the laser closer to the test section to provide light of greater intensity over a smaller area. A 5 mm extension ring for the camera lens produced a field of view which covered roughly 4 cm x 5 cm. The laser was placed so that a section of this size was illuminated, and measurable image traces were obtained. Fields of view larger than this did not produce adequate results.

3.2.3 PIV Procedure

Once the test loop had stabilized for each of the three cases, the following procedure was followed to obtain particle traces. See Figure 3.1 for arrangement of the equipment.

- 1) Turn on light chopper motor, and measure rpm with tachometer until the desired rotation is obtained (1150 rpm). Allow motor to stabilize for approximately 10 minutes.
- 2) Turn on laser and allow it to warm up for approximately 3 minutes. Direct laser light sheet through chopping disk and the desired plane of the test cell.
- 3) Connect CCD camera to the VCR and connect the VCR to a TV monitor.

- 4) Focus CCD camera on a desired section of the light sheet at 90° to the plane of the sheet.
- 5) Darken the room and record 20 - 30 seconds of the particle motion.
- 6) Repeat steps 4 and 5 for all 24 sections of the test cavity.
- 7) Image analysis (see Section 3.1.5)
- 8) Data manipulation (see Section 3.1.6)

CHAPTER 4

RESULTS AND DISCUSSION

4.1 Introduction

An experimental investigation was performed using Particle Image Velocimetry (PIV) to determine the velocity fields of mixed convective flow in a rectangular enclosure. Three cases were investigated, varying both the inlet jet velocity and the wall temperature, and the resulting flow patterns and velocity fields were analysed. Table 4.1 provides information about the three different cases.

Table 4.1 - Summary of Cases

CASE	1	2	3
u_j (m/s)	0.0887	0.0887	0.0377
T_w (°C)	20.7	50.67	80.98
T_1 (°C)	20.7	22.4	27.2
Pr	6.82	4.70	3.29
Re_D	708.3	983.68	574.66
Re_{II} (10^4)	2.631	3.654	2.76
Gr_w (10^3)	0	6.129	30.11
Gr_{II} (10^9)	0	4.903	24.09
Ri_{II}	0	3.694	53.18

All properties evaluated at the film temperature, $T_f = (T_w + T_1)/2$

The parameters of these cases were chosen to duplicate those of Nurnberg [2], with respect to

the heated wall temperature. Case 1 duplicates Nurnberg's [2] case 1 to provide a comparison of dimensionless velocities in the x and y directions for isothermal flow. Case 2 lies between Nurnberg's [2] cases 2 and 3, to provide an intermediate case for comparison of dimensionless velocities and separation heights in the separated flow regime. Case 3 duplicates Nurnberg's case 4 to provide a comparison of dimensionless velocities for the buoyancy-dominated flow regime. Nurnberg [2] selected these cases as they cover the entire range from inertia- to buoyancy-dominated flow regimes.

Experimental results are presented in section 4.2.1 and 4.2.2, which provide qualitative and quantitative information respectively. A comparison of these quantitative results to those found by Nurnberg [2] is presented in section 4.3, and measurement error is discussed in section 4.4. To facilitate the comparison of results from the current and previous work, cavity dimensions and fluid velocities are made dimensionless by the following:

Dimensionless Coordinate:

$$X = \frac{x}{H} \quad Y = \frac{y}{H} \quad (4.1)$$

where H is the height of the test cavity, and x and y are the horizontal and vertical dimensions of the cavity respectively.

Dimensionless Velocity:

$$U = \frac{u}{u_j} \quad V = \frac{v}{u_j} \quad (4.2)$$

where u_j is the inlet jet velocity, and u and v are the horizontal and vertical components of the fluid velocity respectively.

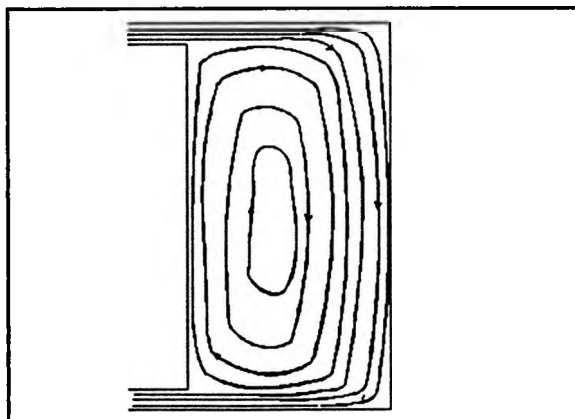
4.2 Experimental Results

4.2.1 Qualitative Results

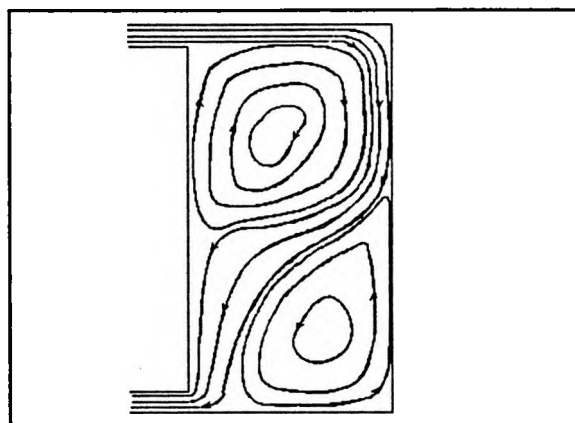
Before quantitative results are presented and comparisons to previous work are made, a brief summary of qualitative results are given to provide a background of the flow regimes encountered in the experiments. Figure 4.1 shows the three flow regimes encountered in the three different cases. These regimes correspond to those found by Nurnberg [2] who used laser induced fluorescence to obtain flow visualization pictures.

The first regime, referred to as "isothermal flow" and shown in Figure 4.1(a), is purely turbulent recirculating flow. The right boundary is not heated in this case. The fluid enters the cavity horizontally along the top boundary, and then turns downward to flow along the right vertical wall. As it meets the bottom boundary, it turns to flow horizontally across the bottom wall toward the outlet. When the fluid reaches the outlet, some fluid exits the cavity and the remainder turns upward to flow along the left vertical wall. As this upward flowing fluid meets the inlet jet, it is entrained into the fluid jet and repeats the above pattern. This motion creates one large clockwise recirculating cell which occupies the entire cavity.

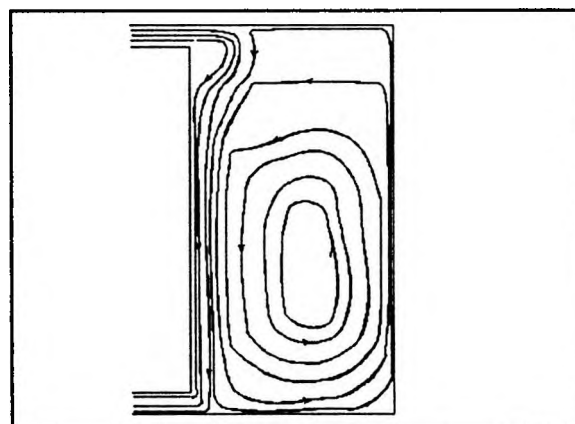
The second regime, shown in Figure 4.1(b) is referred to as "separated flow" [2]. The fluid jet enters the cavity horizontally until it meets the right boundary where it turns downward to flow along the vertical heated wall. At some point however, this inertially-driven flow meets with a buoyancy-driven flow travelling upward along the vertical heated wall. At this point the flow separates from the right vertical boundary, and flows diagonally toward the cavity outlet. The separation height, y_{sep} , is defined as the distance from the point of separation to the bottom of the cavity [2]. As the fluid flows towards the cavity outlet, some turns upward as it meets the left vertical wall and is entrained into the inlet jet at the inlet region. This creates an inertially-driven, clockwise rotating cell in the upper left portion



(a) Isothermal Flow



(b) Separated Flow



(c) Buoyancy-dominated Flow

Figure 4.1 - Observed Flow Regimes

of the cavity. Near the outlet, some fluid exits the cavity, and the remainder turns horizontally to flow along the bottom wall toward the heated vertical wall. Heat is transferred to the fluid as it flows near the heated wall and because it is less dense, rises upward along the vertical wall. As it meets the inertially-driven flow it separates from the wall and flows toward the outlet. This creates a buoyancy-driven, counter-clockwise recirculating cell in the lower right corner of the cavity. The relative size of the two rotating cells is dependent on the Richardson number [2]. For these flow conditions, the Richardson number is calculated as follows:

$$Ri_H = a^2 \frac{Gr_H}{Re_D^2} \quad (4.3)$$

where a^2 is a scaling factor as the Grashof and Reynolds numbers are based on different length scales [2]. Nurnberg [2] also observed a small counter-clockwise rotating cell in the top right corner of the cavity. However in the present work, insufficient light penetrated into this portion of the cavity, and no results were obtained in this region.

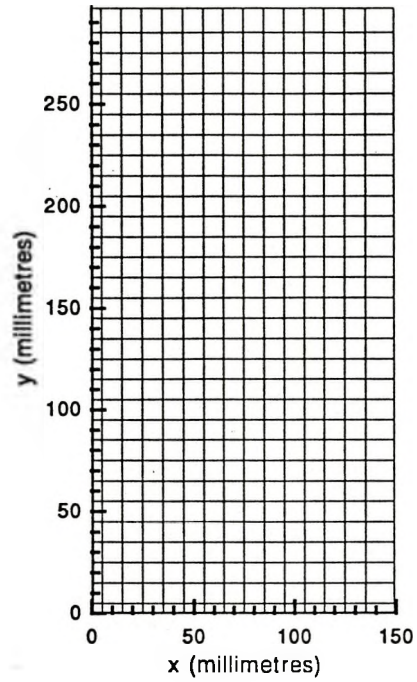
The third flow regime, referred to as "buoyancy-dominated flow" [2], is shown in Figure 4.1(c). The inlet jet enters the cavity and begins to flow horizontally across the upper boundary. However, a large buoyancy-driven, counter-clockwise recirculating cell dominates the cavity, and as the inertially-driven flow meets this cell, the flow separates from the upper boundary and flows downward along the left vertical wall. The distance from this separation point to the inlet is referred to as the "penetration depth", x_{pen} [2]. This flow regime is dominated by the buoyancy-driven cell which occupies nearly the entire cavity.

The isothermal flow regime was observed in Case 1 of the present work. The separated flow regime was observed in Case 2 of the present work and in Case 1 to 3 of Nurnberg [2]. The buoyancy-dominated flow regime was observed in Case 3 of the present

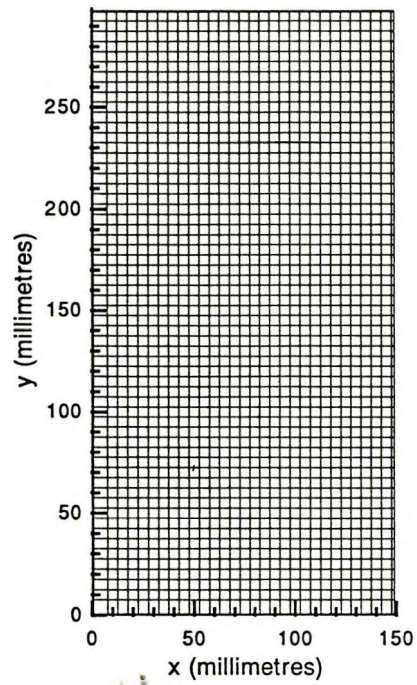
work and Case 4 of Nurnberg [2]. The following trend was observed as the temperature of the heated wall was increased, i.e. the Richardson number was increased. The clockwise inertially-driven cell decreased in size and the counter-clockwise buoyancy-driven cell became larger. As the size of the buoyancy-driven cell increased, the point of separation moved up the heated wall. When the Richardson number was high enough, the buoyancy-driven cell dominated the cavity and the separation point moved up the heated wall and across the upper wall of the cavity. Thus the buoyancy-dominated flow regime may be considered a special case of the separated flow regime [2].

4.2.2 Quantitative Results

Approximately 1900 video frames were analysed to obtain the velocity information presented in this section. For Cases 1, 2, and 3 the number of measured velocity vectors was 1225, 1040, and 640 respectively. Fewer measurements were obtained for Case 3 because in some sections of the cavity the displacement of the particles during the exposure time was not large enough to measure accurately. Data acquisition time was of the order of days, however image analysis required three weeks to complete. In each of the cases, the velocity vectors were recorded at random locations within the flow field. To display the velocity field, the random vectors were averaged onto two different regularly-spaced grids as shown in Figure 4.2 (a) and (b). Grid 2 was made finer than Grid 1 to reveal any small scale fluctuations in velocity. Figures 4.3 to 4.5 present the velocity fields for the three cases, averaged onto Grids 1 and 2. The velocity fields were measured on a x-y plane at a depth of approximately 10 mm from the outside of the cavity. It was expected that the out-of-plane velocity would be small since the depth of the cavity is less than one sixth of the width. Velocity vectors in the upper and lower extremities of the cavity could not be measured, because insufficient light



(a) Grid 1 - Coarse Grid: 1 cm spacing



(b) Grid 2 - Fine Grid: 0.5 cm spacing

Figure 4.2 - Velocity Vector Grids

penetrated into these areas. However, the inlet jet velocity, u_j was found from the volumetric flowrate of the pump and the dimensions of the inlet duct. The velocity vectors in Figures 4.3 to 4.5 are plotted as dimensionless, using the inlet jet velocity as the unit vector.

The results for Case 1 are presented in Figure 4.3 (a) and (b). The velocity measurements are consistent with the isothermal flow regime observed by flow visualization. The majority of the cavity is dominated by one large clockwise rotating cell. The highest velocities (approximately $0.75 u_j$) occur along the right vertical wall and the lower portion of the cavity near the outlet. Near the left vertical wall, the velocities are lower (approximately $0.3 u_j$) because of the effect of gravity on the fluid.

Figure 4.4 (a) and (b) show results for Case 2. Velocity measurements are consistent with flow visualization observations for the separated flow regime. The cavity contains two recirculation cells, one inertially-driven which rotates clockwise and one buoyancy-driven which rotates counter-clockwise. The separation point occurs at a height of approximately 180 mm or 0.61 in dimensionless units. Velocity information in the region of separation is sparse because this region is highly turbulent and the out-of-plane velocity component is significant. Nurnberg [2] found that the separation location oscillated with an amplitude of approximately 5 mm. The current measurements are considered to be steady state as the frames examined to obtain the velocity information were recorded over a period of 1 second. This is assumed to be less than the frequency of the fluctuations in the separation point location.

The highest velocities (approximately $0.6 u_j$) occur in the region between the two cells, as a result of the inertia of the inlet jet. The velocities in the inertially-driven cell are approximately twice as large as those in the buoyancy-driven cell.

Results for Case 3 are presented in Figure 4.5 (a) and (b). The cavity is dominated

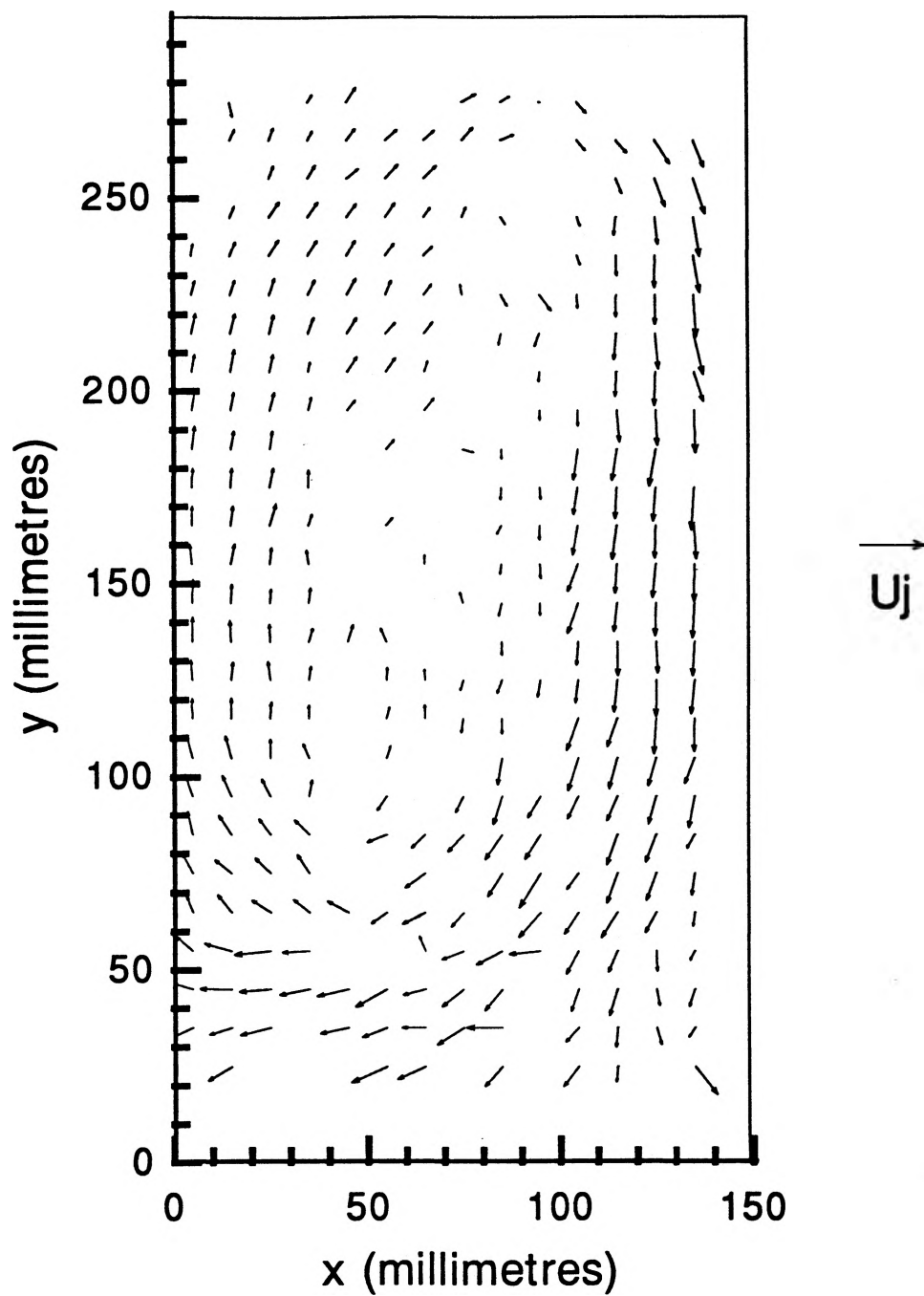


Figure 4.3 (a) - Case 1 PIV Results (Grid 1)

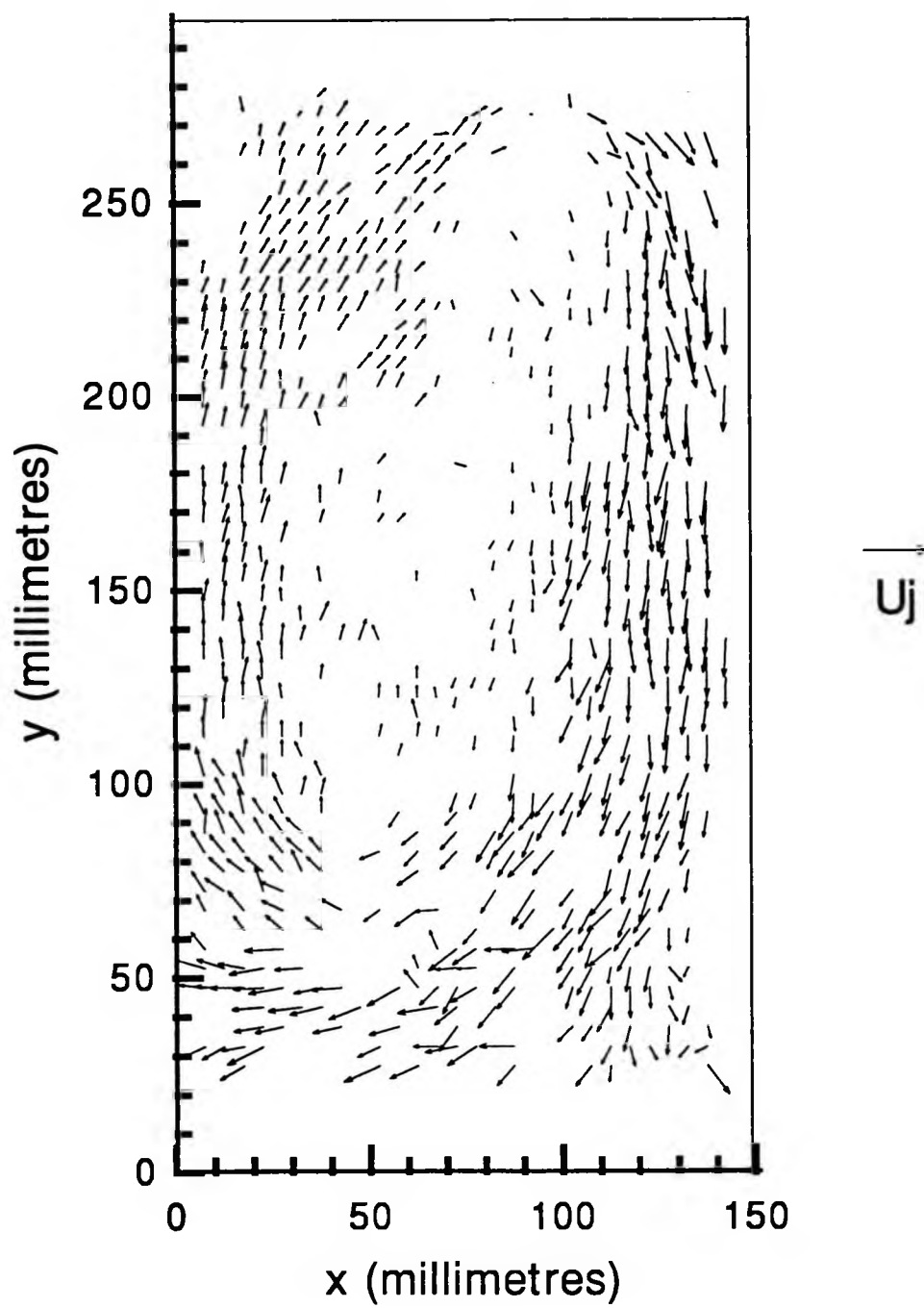


Figure 4.3 (b) - Case 1 PIV Results (Grid 2)

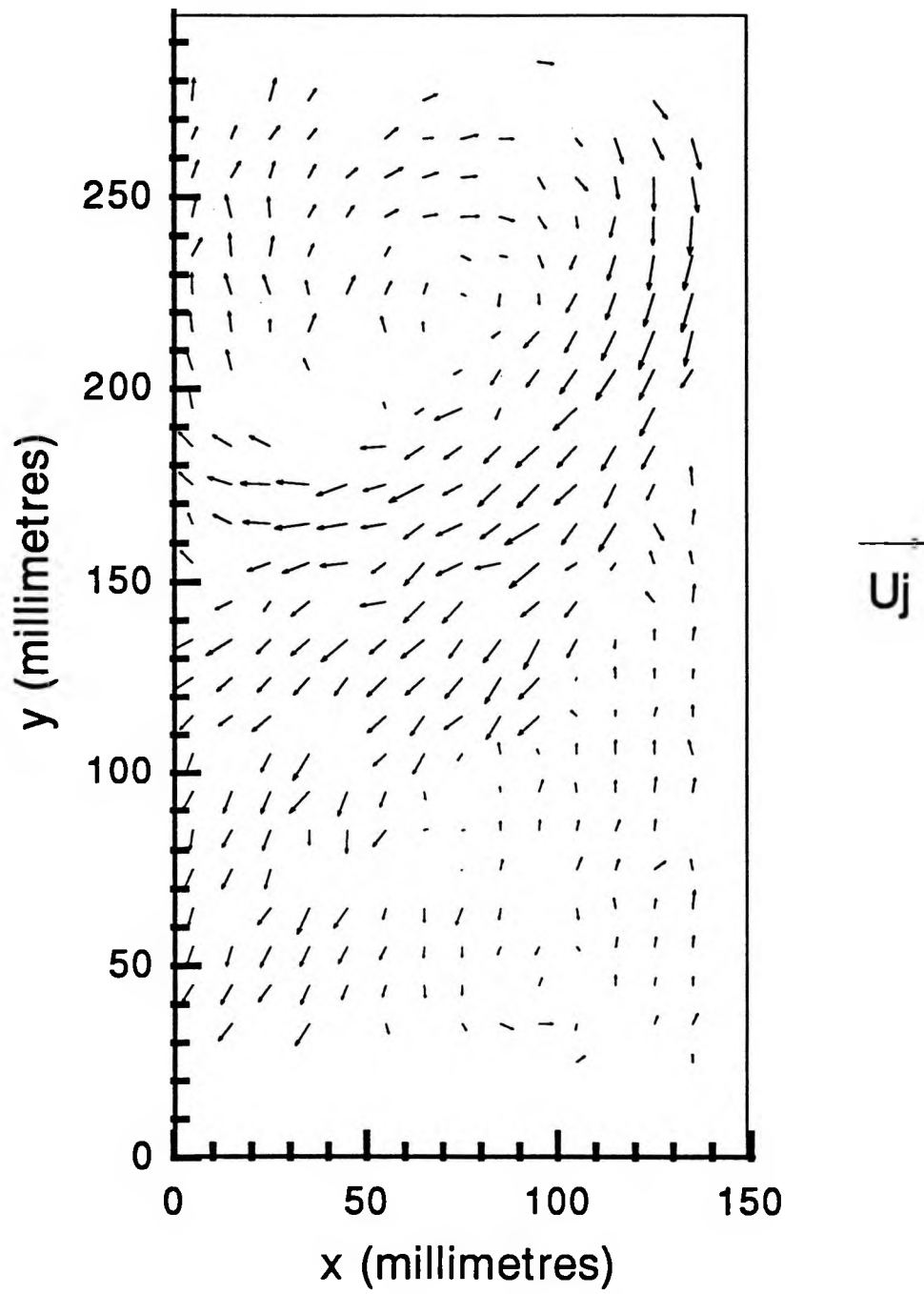


Figure 4.4 (a) - Case 2 PIV Results (Grid 1)

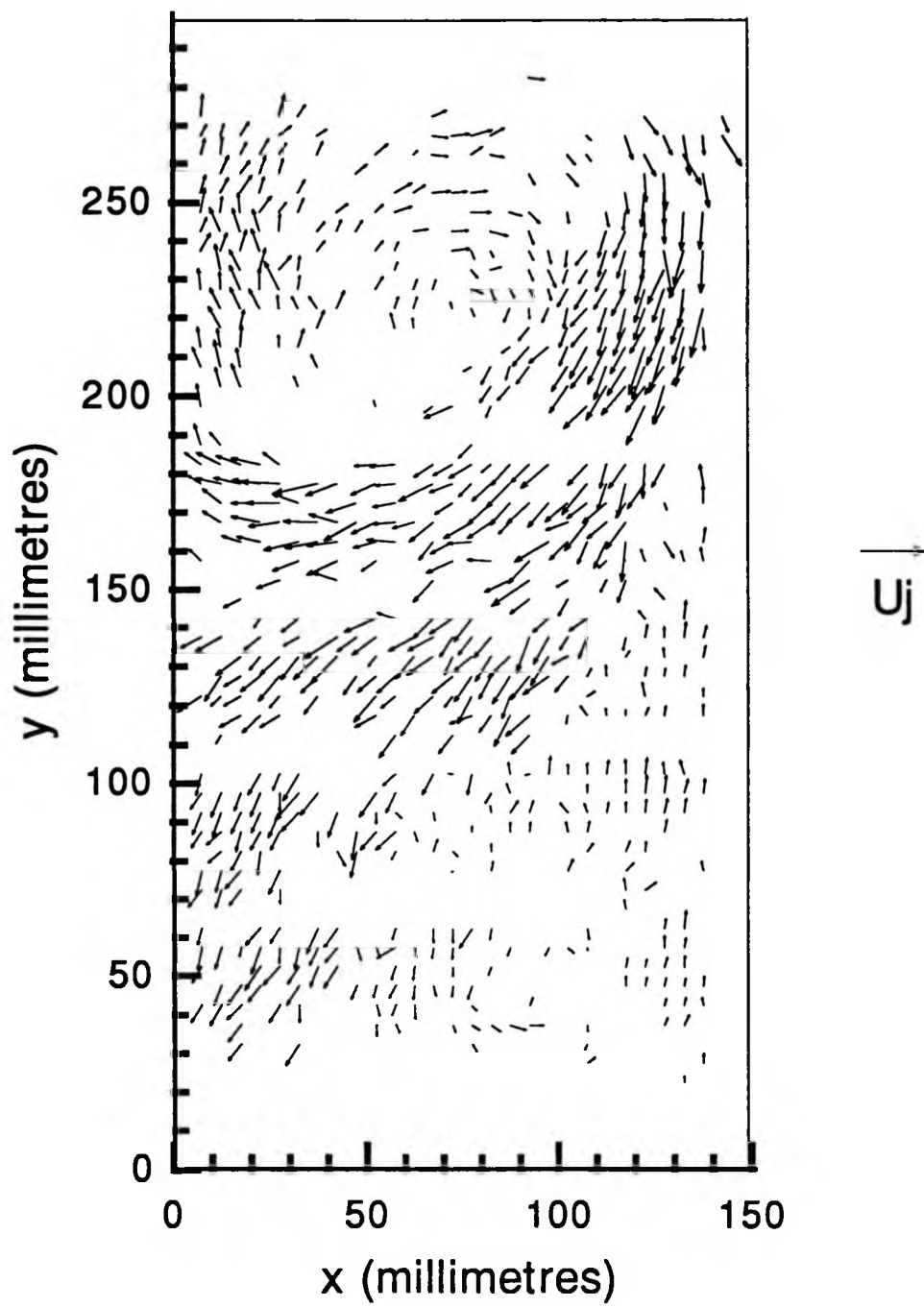


Figure 4.4 (b) - Case 2 PIV Results (Grid 2)

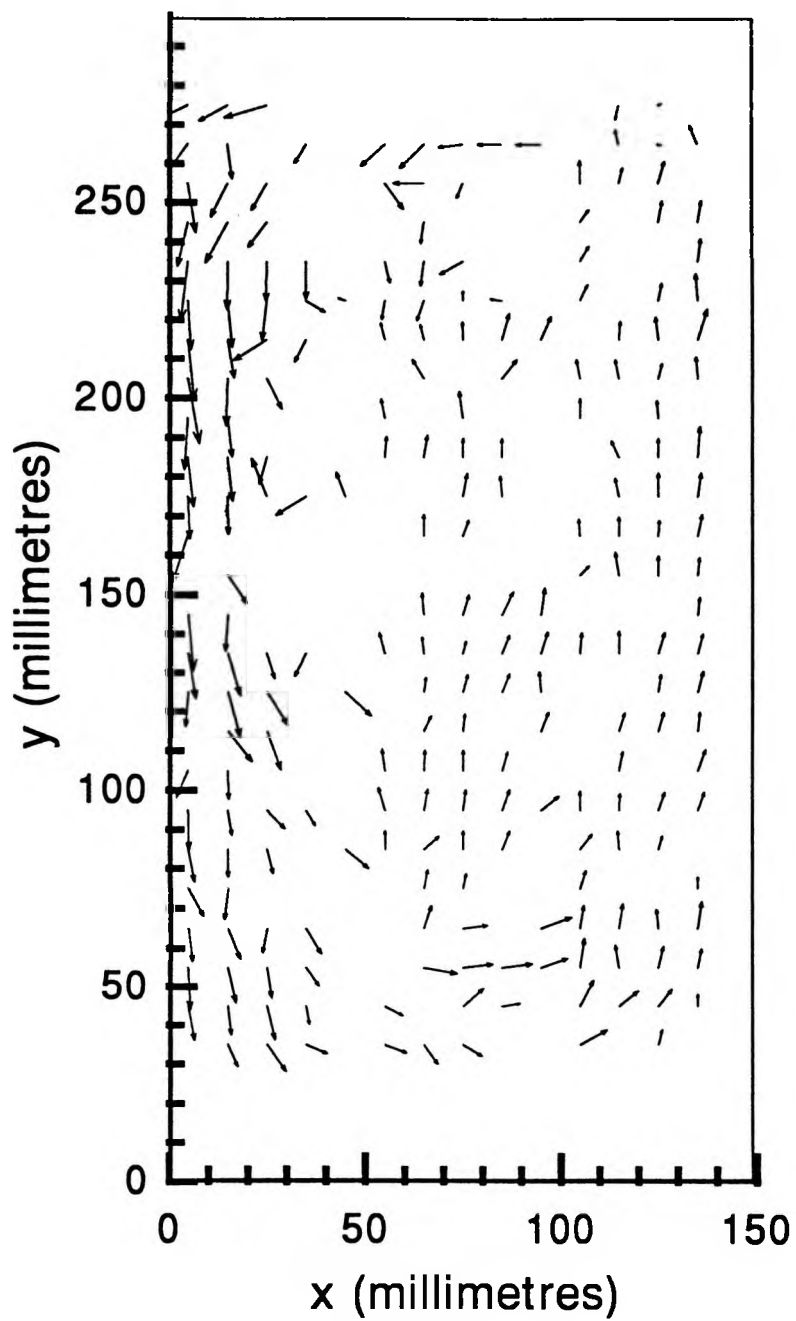


Figure 4.5 (a) - Case 3 PIV Results (Grid 1)

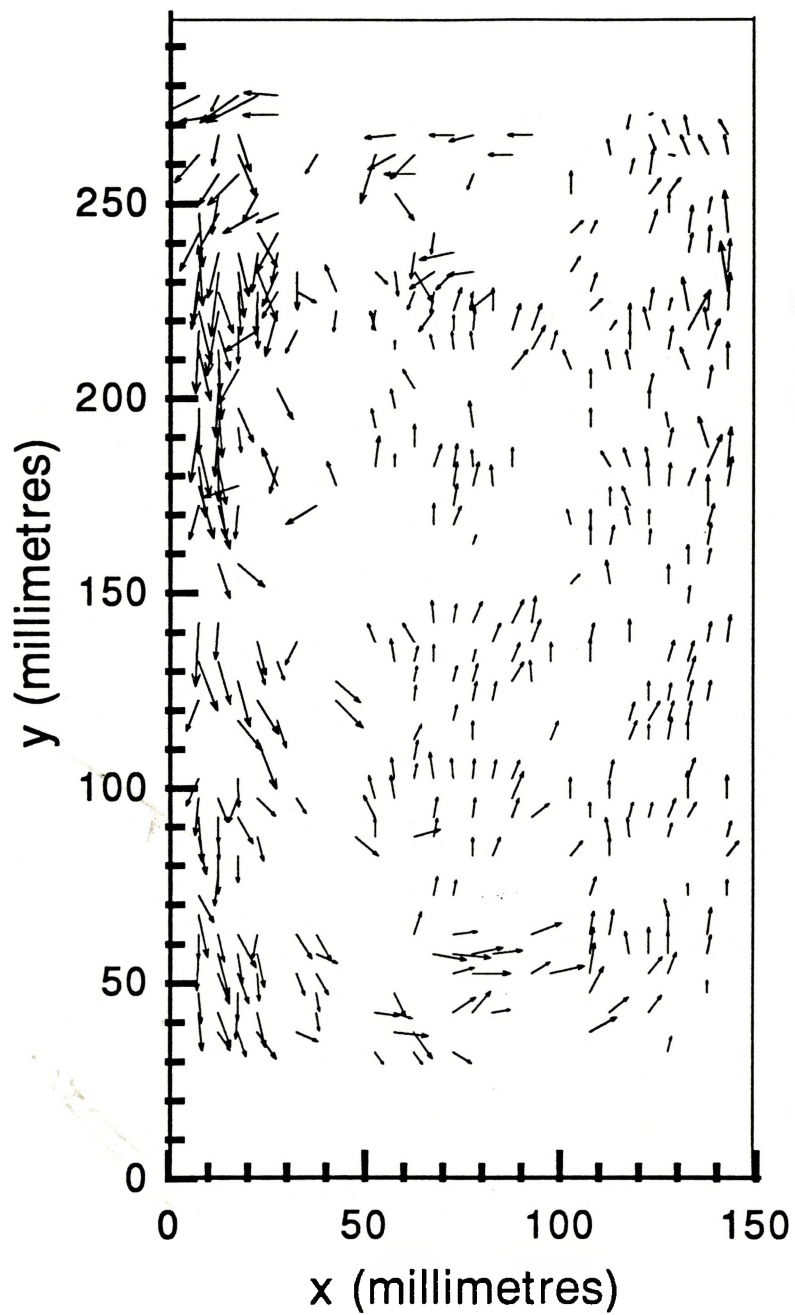


Figure 4.5 (b) - Case 3 PIV Results (Grid 2)

by one large counter-clockwise rotating cell which is consistent with flow visualization information. Heat is transferred to the fluid adjacent to the heated wall and being less dense, flows upward and across the top boundary where it meets the inlet jet. At this point (penetration depth), both the buoyancy-driven fluid and the inlet jet turn to flow toward the bottom of the cavity. As the fluid meets the bottom boundary, the fluid divides with some turning toward the heated wall and the remainder exiting the cavity. The buoyancy-driven cell of Case 2 has increased to dominate the cavity and the separation point has moved across the upper boundary. Lack of light into the test cavity along the upper boundary prohibits the accurate determination of the penetration depth. However, it is estimated to be approximately 10 mm or 0.034 in dimensionless units. The highest velocities (approximately u_i) occur adjacent to the left vertical boundary. This is simply the inlet jet turned downward by the buoyancy-driven counter-clockwise rotating cell. For practical considerations, it must be noted that the "cooling" fluid does not reach the heated surface.

4.3 Comparison to Previous Work

In this section, comparisons are made between the current experimental data and the experimental and numerical results found by Nurnberg [2]. Direct numerical comparisons between the cases of the present work and those of Nurnberg [2] are not possible, except in the cases involving isothermal flow, because of large differences in Richardson number. It is expected that discrepancies will arise because of this, however general trends in the measurements can be compared. Case 1 of the present work is compared to Case 1 of Nurnberg [2], as they both involve isothermal flow. A comparison of the experimental vertical velocity near the heated wall is presented. For the separated flow regime, the results of Case 2 are compared to Nurnberg's [2] Cases 2 and 3. Although all three cases involve

separated flow, each is characterized by a different Richardson number. A comparison of experimental separation heights is made, and the present velocity profiles along the vertical and horizontal centrelines of the cavity are compared to the experimental results found by Nurnberg [2]. Finally, for the buoyancy-dominated flow regime, experimental velocity results of Case 3 are compared to numerical predictions of Case 4 of Nurnberg [2], and experimental penetration depths for the two cases are compared. Again, though these cases involve buoyancy-dominated flow, they differ in Richardson number. Comparing the present experimental results to Nurnberg's [2] experimental results gives an indication of the accuracy and applicability of the PIV technique. If the PIV technique is proven to be comparable to LDA with respect to its accuracy, then a comparison of the present experimental results to Nurnberg's [2] numerical predictions provides additional verification of his numerical code.

Figure 4.6 compares the vertical velocity near the right vertical wall for the isothermal cases. At a depth of 10 mm from the outside wall, good correlation is found between results obtained using LDA [2] and PIV, except near the bottom boundary. LDA measurements show very small positive velocities in this region, which is consistent with the existence of a small counter-clockwise recirculation cell in the bottom right corner of the cavity. Velocities measured with PIV are larger and negative in this area. As stated previously, this recirculation cell was not observed in the PIV analysis.

Figure 4.7 plots the vertical velocity profile along the horizontal centreline of the cavity, for Case 2 of the present work, and the experimental results of Case 2 of Nurnberg [2]. Large discrepancies are apparent between the present work and Nurnberg's [2] results, however it must be realized that conditions in Case 2 of the present work correspond to a Richardson number of 3.69, whereas in Case 2 of Nurnberg [2] it is 1.27. This difference in Richardson number results in two flow patterns, which differ in separation height and in the

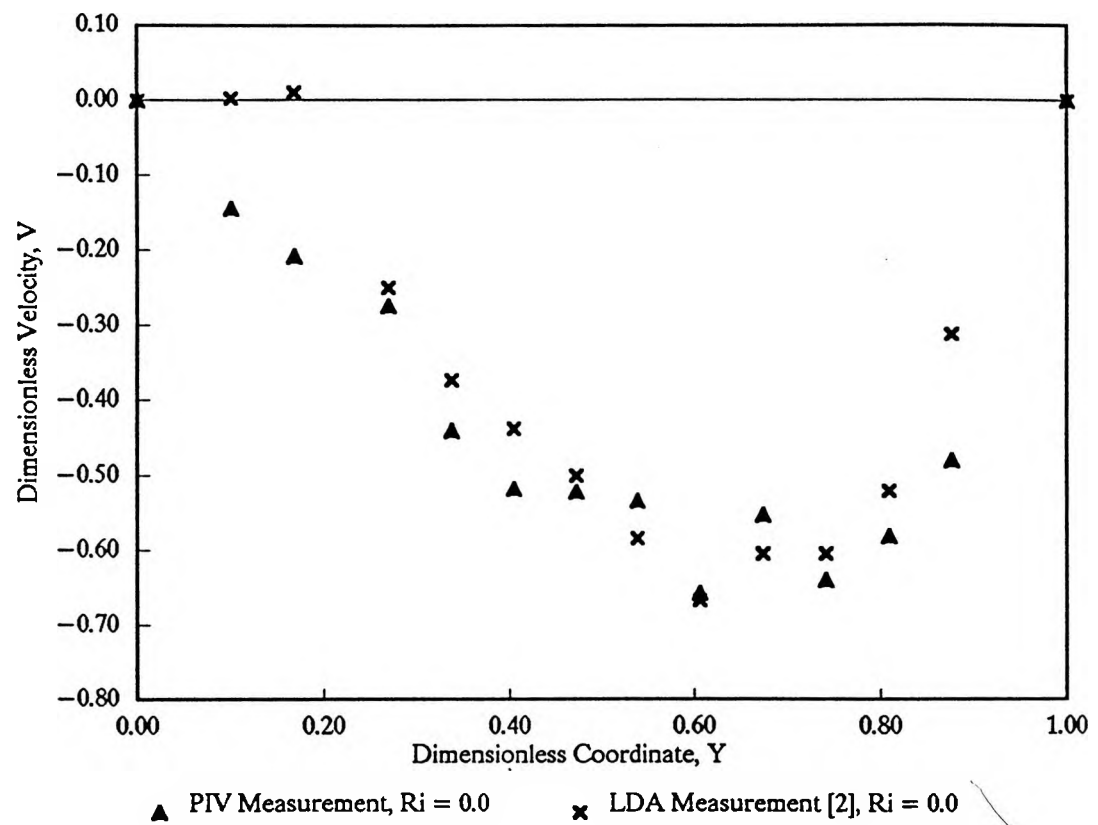


Figure 4.6 - Isothermal Flow - Vertical Velocity Near Heated Wall

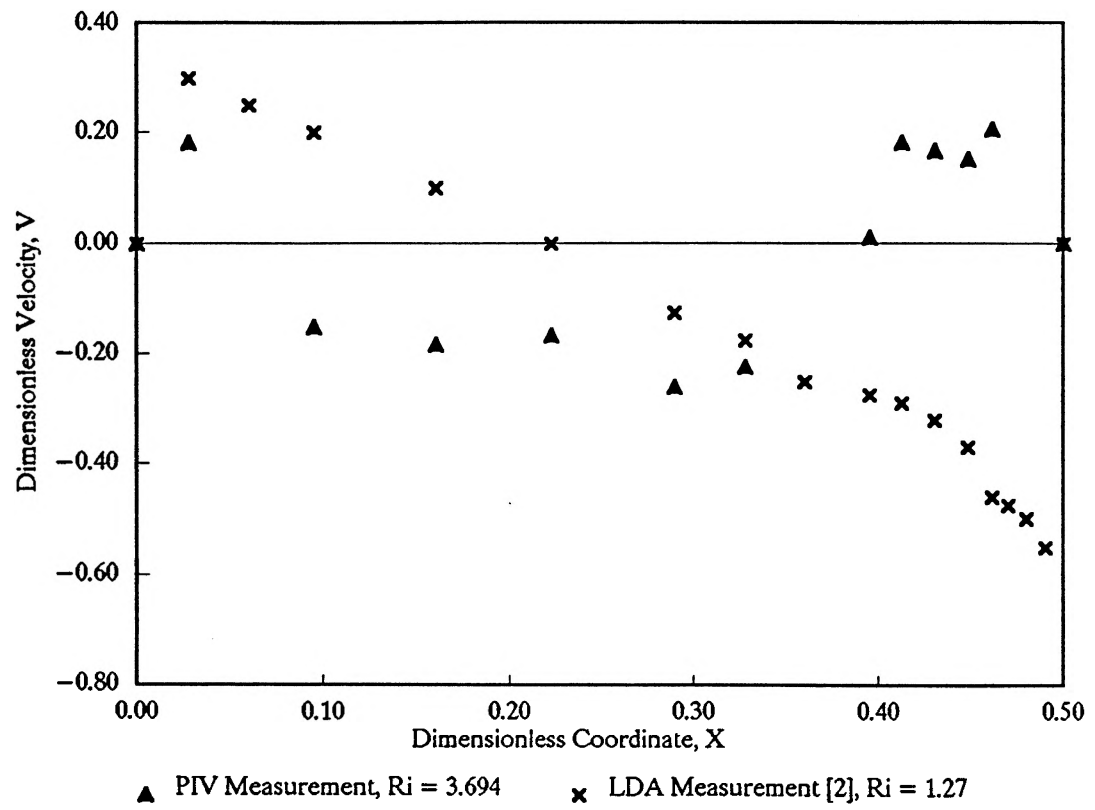


Figure 4.7 - Separated Flow - Vertical Velocity Profiles along Horizontal Centreline

size of the recirculation cells. Better agreement is seen in Figure 4.8, where the vertical velocity profile at a height of 0.76 dimensionless units is compared to that at the horizontal centreline of Nurnberg's [2]. Visually and numerically, the velocity profile at this height is similar to that at the horizontal centreline of Nurnberg's [2].

In comparing the horizontal velocity profiles along the vertical centreline of the cavity for the above cases, large discrepancies are again apparent for the reasons mentioned above.

In Figure 4.9, the experimental horizontal velocity profile along the vertical centreline of the cavity from Case 2 of Nurnberg [2] is plotted with the horizontal velocity profile at 0.11 dimensionless units (in the x direction) of the present work. At this position, the profile closely agrees with that of Nurnberg at the vertical centreline of the cavity, except near the top boundary. PIV measurements were not possible near the top of the cavity as the laser light did not penetrate into this region. Small discrepancies are also apparent in the central region of the cavity. This may be due to the difference in flow patterns between the two cases.

A comparison of dimensionless separation locations is given in Table 4.2. The separation height of Case 2 of the present work is compared to those in Cases 1, 2 and 3 of Nurnberg [2].

Table 4.2 - Summary of Dimensionless Experimental Separation Locations

CASE	u_j (m/s)	T_w (°C)	Ri_{II}	y_{sep}
2	0.0887	50	3.694	0.60
1 [2]	0.124	20	0	0.24
2 [2]	0.123	40	1.27	0.40
3 [2]	0.063	60	11.9	0.64

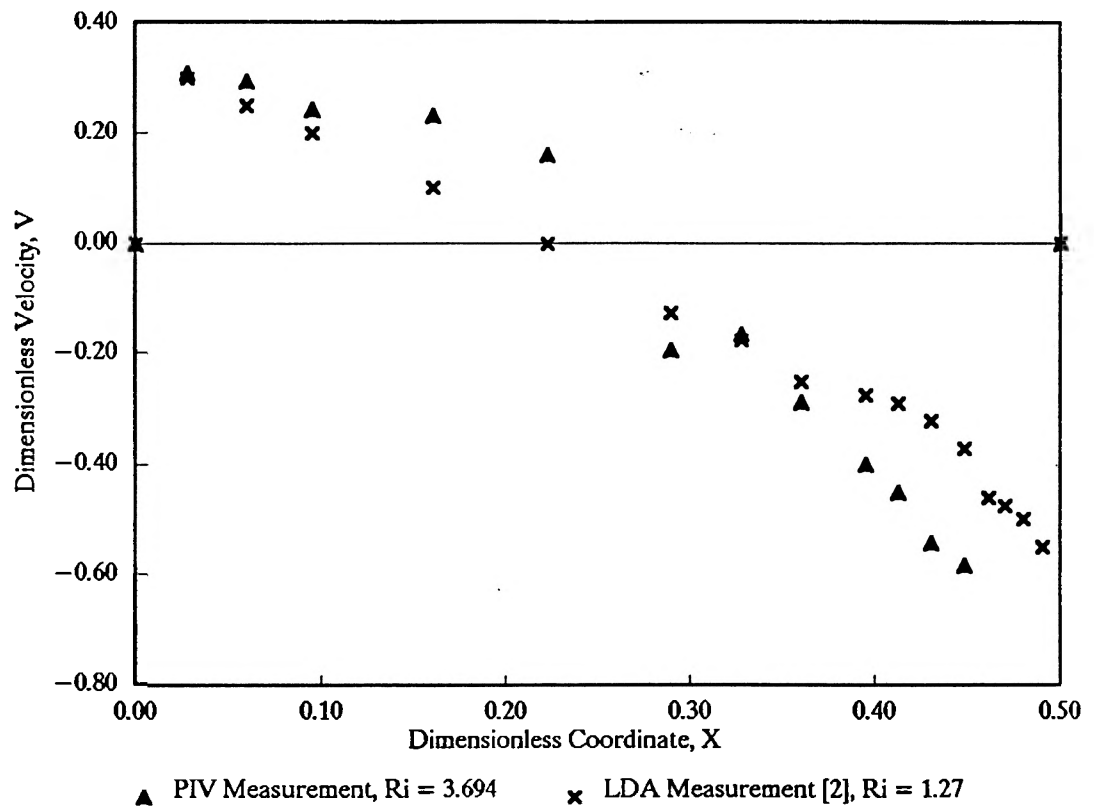


Figure 4.8 - Separated Flow - Vertical Velocity Profile Comparison

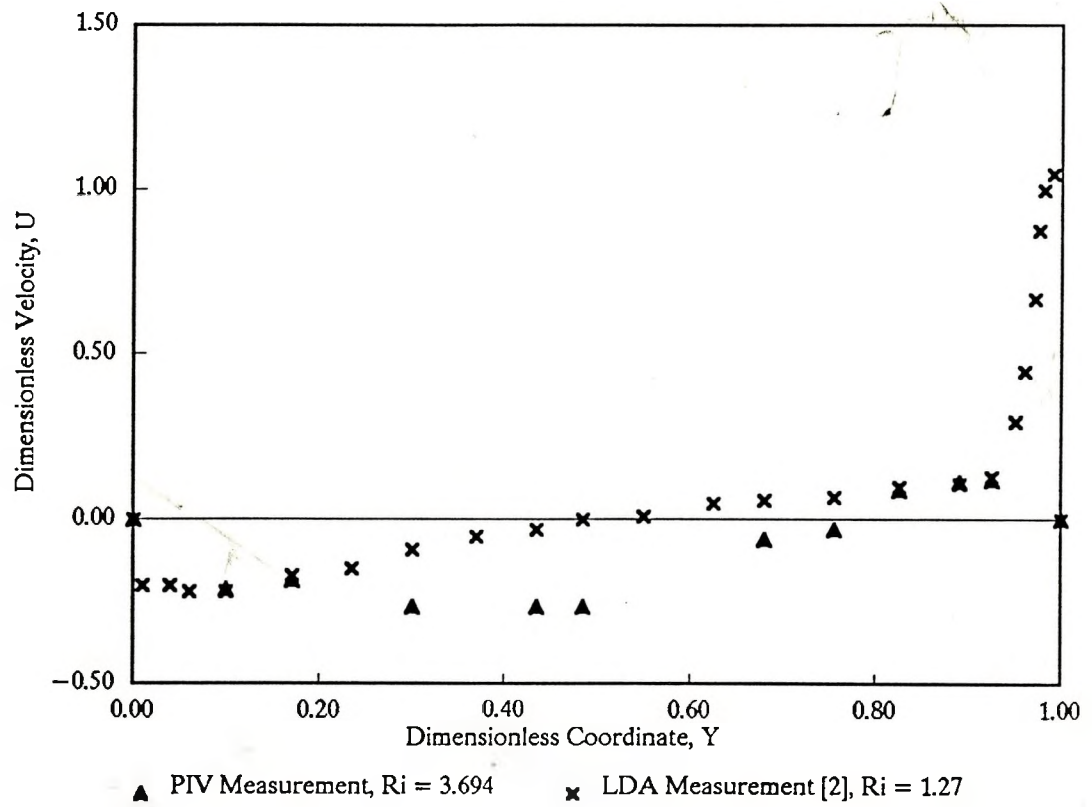


Figure 4.9 - Separated Flow - Horizontal Velocity Profile Comparison

In general, the separation location increases with increasing wall temperature and decreases with increasing inlet jet velocity. The separation location is dependent on the Richardson number since it combines these two flow parameters. Although the temperature of the heated wall is increased linearly, the separation height does not follow this trend because it also depends on the inlet jet velocity which is different for each of the cases. From Cases 1 and 2 of Nurnberg [2], for nearly identical inlet jet velocities, a change in wall temperature of 20°C causes the separation point to move upward by 0.16 dimensionless units. In Case 3 of Nurnberg [2], if an inlet jet velocity of 0.123 m/s were used, the separation point would be expected to move upward by 0.16 dimensionless units to 0.56 dimensionless units. However, the actual measured location for this case is higher (0.64 dimensionless units) because the inlet jet velocity is only 0.063 m/s. Less inertia is present to drive the separation point down the heated wall. The same analysis can be applied to Case 2 of the present work. If an inlet jet velocity of 0.123 m/s were imposed, the separation point would be expected to move upward, but by 0.08 dimensionless units since the wall temperature only changed by 10°C . This expected separation location of 0.48 dimensionless units is much lower than the actual measured location of 0.60 dimensionless units because a lower inlet jet velocity is used and less inertia is present. It can be concluded that the separation location of Case 2 of the present work is consistent with the results of Nurnberg [2].

In Figure 4.10, vertical velocity profiles along the horizontal centreline are plotted for Case 3 of the present work and the numerical predictions of Nurnberg's [2] Case 4. In general, the trends are similar. However, the vertical velocity at the left wall is slightly less than predicted, and the velocities in the central core of the cavity are slightly larger than predicted. Again it must be realized that the cases differ in Richardson number, and therefore they differ in flow pattern.

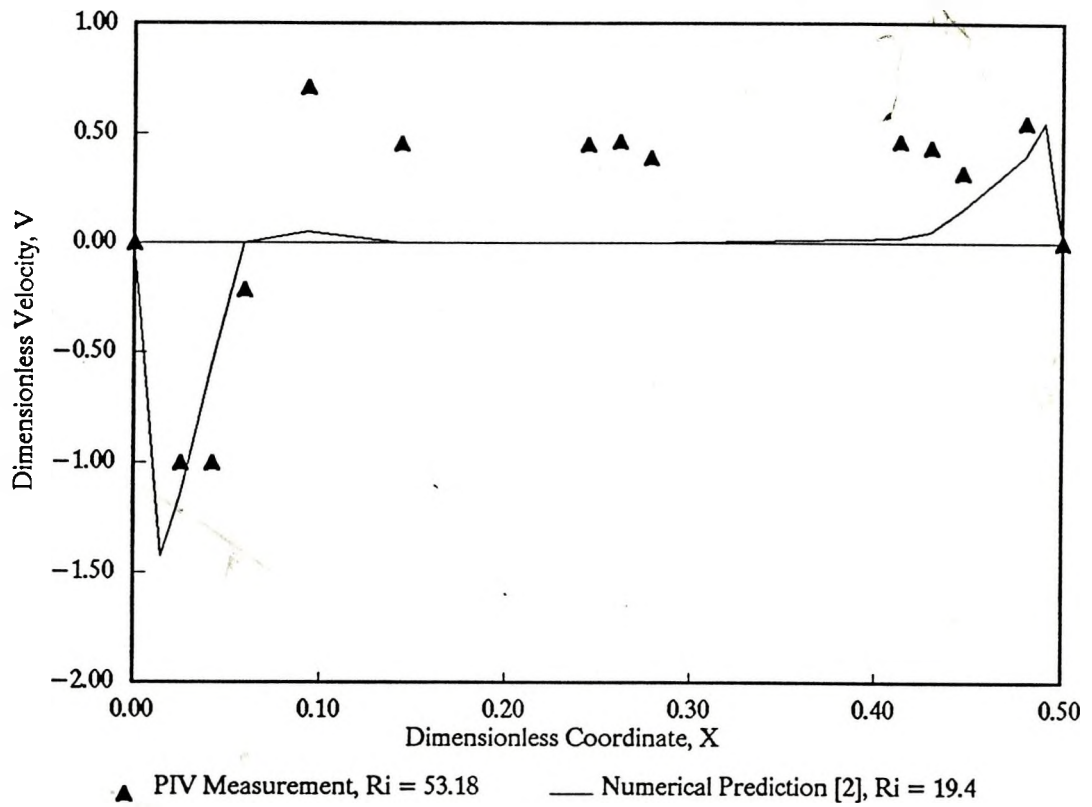


Figure 4.10 - Buoyancy-dominated Flow - Vertical Velocity Profiles along Horizontal Centreline

Horizontal velocity profiles along the vertical centreline of the cavity are plotted for these cases in Figure 4.11. Good agreement is found in the central core of the cavity however, measured velocities near the top and bottom boundaries are much higher than numerically predicted values.

Table 4.3 compares experimental penetration depths of the two buoyancy-dominated cases. This comparison reveals that in the present work, the fluid jet penetrates approximately half the distance of that in Nurnberg's [2] Case 4. This is expected since the inlet jet velocities of the two cases are similarly related.

Table 4.3 - Summary of Dimensionless Experimental Penetration Depths

CASE	u_j (m/s)	T_w ($^{\circ}$ C)	Ri	x_{pen}
3	0.0377	80	53.18	0.034
4 [2]	0.063	80	19.4	0.083

4.4 Measurement Error

Through the comparison of PIV results to those obtained using LDA, some observations can be made as to the accuracy of the PIV technique. In general, the results of the PIV experiments are consistent with LDA measurements performed by Nurnberg [2]. There are however, some apparent discrepancies in the velocity fields obtained using the two different methods. These discrepancies can be attributed to the differences in flow patterns, and the measurement error and limitations involved in this PIV system and the PIV technique in general. Since the measurement of particle displacement was made manually, some error is involved in the ability to accurately determine the beginning and end of the particle trace. This is inhibited by blurring and the finite spatial resolution of the recorded image. The

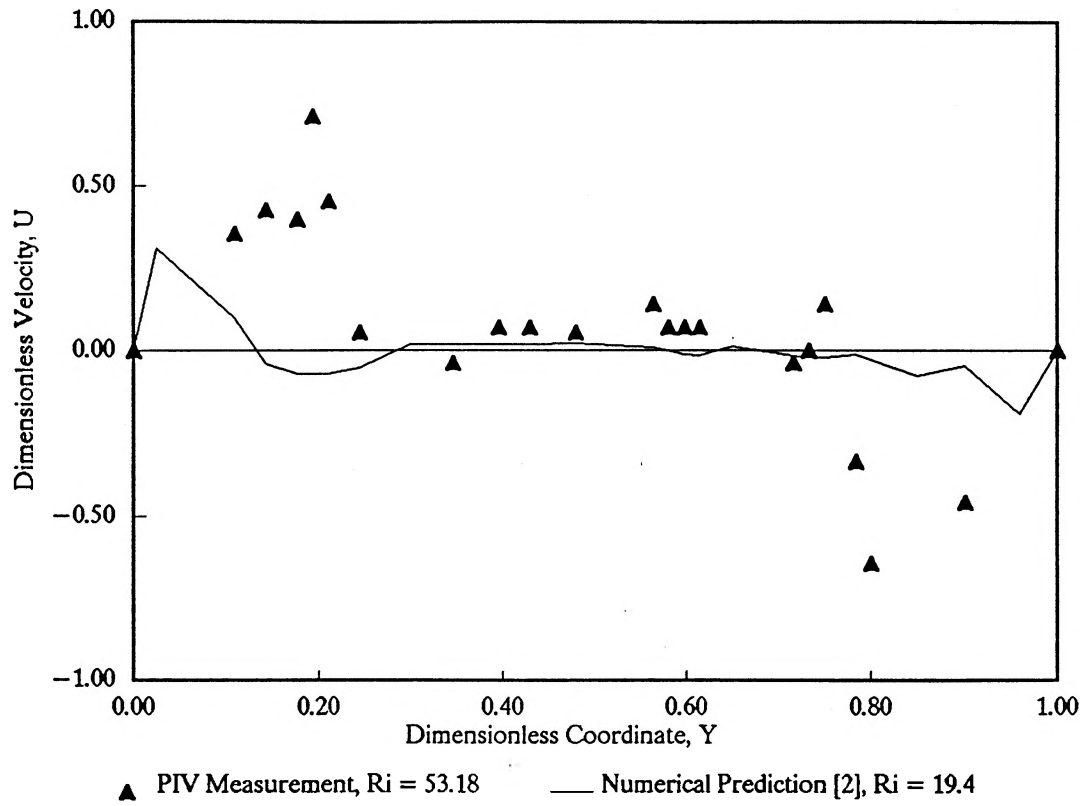


Figure 4.11 - Buoyancy-dominated Flow - Horizontal Velocity Profiles along Vertical Centreline

determination of the total exposure time is subject to error since there is some variation in the speed of the motor which turns the light chopping disk. The accuracy of the tachometer measurement is to within ± 1 RPM for 5 to 5000 RPM, and this error is considered negligible in determining the total exposure time.

One limitation of this particular PIV system is that it has a low dynamic range. The range of velocities that it can accurately measure is limited by the source of illumination and method of interruption used. Since the intensity of the laser light is low, large exposure times are required to produce images of sufficient quality. Large exposure times result in large particle displacements. This reduces the accuracy of the velocity measurement, because measurement accuracy decreases as the particle displacement increases. This laser also increases data acquisition and analysis time because recording and image analysis have to be performed in small sections. Normally, the entire flow field is recorded and analysed instantaneously. Although it was assumed that the flow conditions were at steady state, errors may have arisen due to the fact that the flow field was not measured instantaneously, but rather in small sections over a period of minutes. With this system, the exposure time could not be made long enough to produce sufficient particle traces in areas where the velocity was very low. This resulted in low data density in these areas. Clearly, the use of a high-intensity pulsed laser would improve the dynamic range and accuracy of this PIV system.

Other factors may have contributed to the discrepancies in the measurements. The procedure of averaging the random velocity vectors onto the grids may have introduced some error. The lens of the CCD camera may not have been aberration free, which would lead to distortion of the recorded images. Imperfections in the glass cylindrical rod used to create the light sheet may have caused distortions in the thickness and intensity of the sheet, which would result in poor quality images.

A limitation of the PIV technique in general is that velocity measurements are impossible to obtain where light does not illuminate the flow. The technique is limited to applications where it is possible to create a test facility which can be completely illuminated. PIV should also be limited to applications where the range of velocities in the flow field is small.

Although the results obtained in the PIV analysis are fairly consistent with those found using LDA, because of the large error involved in this PIV system, verification of the Nurnberg's [2] numerical code is not possible. Although this objective was not met, this investigation does provide useful information about the PIV technique to aid in the design of a more accurate system. Using this information, recommendations are made in the final chapter for the design and assembly of a superior PIV system for future work.

CHAPTER 5

CONCLUSIONS AND RECOMMENDATIONS

5.1 Conclusions

An investigation was performed to determine the velocity fields of mixed convective flows in a rectangular enclosure of aspect ratio 2. Velocity fields were determined with a technique called Particle Image Velocimetry (PIV). The PIV system was assembled from readily-available components to investigate the applicability and performance of the PIV technique while keeping costs to a minimum. When compared to previous experimental data, it was found that without sophisticated equipment, the technique is not as accurate as other optical measurement methods such as LDA. This is the one major drawback of the PIV technique; a system that will provide accurate measurements is expensive to construct and operate. Recommendations for such a system are given in the following section.

The present PIV system was found to be inadequate in accurately determining velocity fields. Its low dynamic range prohibits the measurement of large velocity gradients. Performing image analysis manually introduces significant error into the velocity measurements. The limited intensity of the light source increases data acquisition and image analysis time, as they are performed in sections. Since the principal idea behind the PIV technique is that the entire velocity field is measured instantaneously, the present PIV system is not entirely correct and further increases the error in measurement. Clearly, improvements must be made and further experiments performed to determine the performance of the PIV technique in general.

From past applications of PIV, it can be concluded that the PIV technique is applicable to many situations, but accurate measurements are obtained only when highly sophisticated equipment is used and extreme care is taken in experimentation.

5.2 Recommendations

Although the experimental results found in this investigation were not used to verify Nurnberg's [2] numerical code, the knowledge gained through performing the experiments and analysis is used to recommend components of an accurate PIV system.

The two main problems of the present PIV system that must be addressed are the light source and the method of image analysis. These components introduce the largest amount of error and determine the dynamic range of the system. They will also comprise the majority of the cost of the improved system.

A high-intensity pulsed laser is recommended to replace the low power continuous wave laser and light chopping disk. In order to freeze particle motion, very short exposure times are required, and the production of good quality particle images requires that the light be of high intensity. Nd:Yag or Argon-ion pulsed lasers produce the required intensity (at least 0.5 mW per pulse), and usually allow the pulse width and separation time to be varied. Variation of these parameters increases the dynamic range of the system. Pulsed lasers also have the ability to respond to an initiating trigger, so that exposure time and camera frame can be synchronized. Although pulsed lasers of this type are very expensive, previously-owned lasers in good condition can be purchased at a reduced price, approximately \$10-15,000.

Manual image analysis is both time-consuming and inaccurate. To replace this, a commercially available software package is recommended. Alternatively, software could be

written using methods defined in Section 2.2.4. TSI Incorporated distributes PIV analysis software called Insight™, which is available in personal computer- and UNIX-based formats. The software acquires a PIV image obtained by either a photographic camera or an on-line video camera, divides the image into small regions and carries out an autocorrelation algorithm on the particle images to determine the particle displacement. The time between exposures and the particle displacement are then used to calculate the velocity for each region, and the process is repeated for the entire image. This software allows the user to enhance poor quality images and to choose the processing algorithm. It automatically validates vector data, removes bad vectors, performs vector scaling, in addition to computing and displaying vorticity and strain rates. The personal computer version requires an i486-based microcomputer equipped with 8 MB of RAM, a frame grabber board, an SVGA monitor, and Microsoft Windows 3.1 operating system. If this software is not used on-line, a VCR is also required to record images for later analysis. The software itself is priced at \$8,000 for the PC version and \$10,000 for the UNIX version.(American funds) A computer equipped as described above would cost approximately \$4,200, (\$2,000 for frame grabber) and the optional VCR would cost approximately \$600.

Additional purchases include a CCD video camera such as the one used in the present work, cylindrical lenses to create the light sheet, and equipment to synchronize the laser pulses with the camera frames. A suitable CCD camera equipped with a 50 mm lens would cost approximately \$1,900, and cylindrical lenses approximately \$2000. TSI also manufactures a LaserPulse™ synchronizer which varies the width and separation of the laser pulses, and synchronizes the pulses with the camera frames. The synchronizer is priced at \$5000 (American funds) .

The total cost of the improved PIV system is approximately \$40,000. Clearly, an

accurate PIV system comes with a high price tag. However, its range of applicability is large and the future use of the system is practically unlimited. The accuracy of this system would be close to that of an LDA system, but at less than half the cost, and requiring less data acquisition and analysis time. It is hoped that a PIV system will be constructed and further experimentation performed, as it will benefit future research in fluid mechanics at McMaster University.

REFERENCES

1. Adrian, R.J., "Multi-point optical measurements of simultaneous vectors in unsteady flow - a review", *Int. J. of Heat and Fluid Flow*, Vol. 7, No. 2, pp. 27- 45, 1986.
2. Nurnberg, G., "An Experimental and Numerical Investigation of Mixed Convection in Rectangular Enclosures", Ph.D. Thesis, McMaster University, 1994.
3. Adrian, R.J., "Particle-imaging techniques for experimental fluid mechanics", *Annual Review of Fluid Mechanics*, Vol. 23, pp. 261-304, 1991.
4. Walter, J.A. and C.J. Chen, "Development of a Quantitative Velocity Measurement System and Its Application to Offset Channel Flow", IIHR Report No. 338, Iowa Institute of Hydraulic Research , University of Iowa, Iowa City, IA, 1992.
5. Buchhave, P., "Particle Image Velocimetry - Status and Trends", *Experimental Thermal and Fluid Science*, Vol. 5, pp. 586-604, 1992.
6. Adrian, R.J. and C.-S. Yao, "Pulsed laser technique application to liquid and gaseous flows and the scattering power of seed materials", *Applied Optics*, Vol. 24, No. 1, pp. 44-52, 1985.
7. Chen. L.J., Ramiro H. Bravo and C.-J. Chen, "Full-Field Velocity Measurement and Numerical Simulation of Flow in a Cubic Chamber", ASME Winter Meeting, Atlanta, Georgia, Dec 1-6, 1991.
8. Willert, C.E. and M. Gharib, "Digital particle image velocimetry", *Experiments in Fluids*, Vol. 10, pp. 181-193, 1991.
9. Grant, I. and G.H. Smith, *Modern Developments in Particle Image Velocimetry, Optics and Lasers in Engineering*, Vol. 9, pp. 245-264, 1988.
10. Farrell, P.V., "Particle Sizing and Velocity Measurements Using Particle Image Velocimetry", FLUCOME'91, 3rd Triennial Symposium on Fluid Control, Measurement and Visualization, Aug. 28-31, 1991, San Francisco, CA.
11. Arroyo, M.P., M. Quintanilla and J.M. Saviron, "Three-Dimensional Study of Rayleigh-Beynard Convection by Particle Image Velocimetry", *Experimental Thermal and Fluid Science*, Vol. 5, pp. 216-224, 1992.
12. Dong, R., S. Chu, and J. Katz, "Quantitative Visualization of the Flow within the Volute of a Centrifugal Pump. Part A:Technique", *Journal of Fluids Engineering*, Vol. 114, pp. 390-395, 1992.

13. Hassan, Y.A. and T. Blanchat, "Flow velocity measurements using digital pulsed laser velocimetry", *Optical Engineering*, Vol. 30, No. 8, pp. 1220-1227, 1991.
14. Hassan, Y.A. and R.E. Canaan, "Full-field bubbly flow velocity measurements using a multiframe particle tracking technique", *Experiments in Fluids* 12, pp. 49-60, 1991.
15. Hassan, Y.A., T.K. Blanchat, C.H. Seeley and R.E. Canaan, "Simultaneous Measurements of Both Components of a Two-Phase Flow using Particle Image Velocimetry", *International Journal of Multiphase Flow*, Vol. 18, No. 3, pp. 371-395, 1992.
16. Kim, Y.-G. and D.-J. Chen, "Quantitative Flow Measurement and Numerical Simulation of Lid-Driven Rotating Cavity Flow", *FED Vol. 143/HTD Vol. 232*, pp. 57-67, 1992.
17. Grant, I., E. Owens, Y.Y. Yan, and X. Shen, PIV measurements of the separated flow behind a rearward facing step, *Experiments in Fluids* 12, pp. 238-244, 1992.
18. Wozniak, K. and G. Wozniak, "Particle-image-velocimetry applied to thermocapillary convection", *Experiments in Fluids*, Vol. 10, pp. 12-16, 1990.
19. Towers, C.E., P.J. Bryanston-Cross and T.R. Judge, "Application of particle image velocimetry to large-scale transonic wind tunnels", *Optics and Laser Technology*, Vol. 23, No. 5, pp. 289-295, 1991.
20. Bergé, P. and M. Dubois, Rayleigh-Bénard Convection, *Contemp. Physics*, 25, pp. 535-582, 1984.
21. Arroyo, M.P. and C.A. Greated, "Stereoscopic particle image velocimetry", *Measurement Science Technology*, Vol. 2, pp. 1181-1186, 1991.
22. Kasagi N. and K. Nishino, "Probing Turbulence with Three-Dimensional Particle-Tracking Velocimetry", *Experimental Thermal and Fluid Science* 4, pp. 601-612, 1991.
23. Kasagi, N., M. Hirata, K. Nishino, N. Ninomiya, and N. Koizumi, "Three-Dimensional Velocity Measurement via Digital Image Processing Technique (in Japanese)", *J. Flow Visualization Soc. Jpn.*, Vol. 7, No. 26, pp. 283-288, 1987.
24. Nishino, K., N. Kasagi and M. Hirata, "Three-Dimensional Particle Tracking Velocimetry Based on Automated Digital Image Processing", *ASME J. Fluids Eng.*, Vol. 111, No 4, pp. 384-391, 1989.
35. Sata, Y., K. Nishino, and N. Kasagi, "Whole Field Measurement of Turbulent Flows Using a Three-Dimensional Particle Tracking Velocimeter", in Flow Visualization V, R. Reznicek, Ed., pp. 248-253, Hemisphere, Washington, D.C., 1990.
26. Nishino, K., and N. Kasagi, "Turbulence Statistics Measurement in a Two-Dimensional Channel Flow Using a Three-Dimensional Particle Tracking

- Velocimeter", Proc. Seventh Symp. Turbulent Shear Flows, Stanford, pp. 22.1 - 22.1.6, 1989.
27. Kasagi, N., N. Ninomiya, and M. Hirata, "Three-Dimensional Velocity Measurement in a Turbulent Jet by Digital Image Processing", in Experimental Heat Transfer, Fluid Mechanics and Thermodynamics, R.K. Shar, E.N. Ganic, and K.T. Yang, Eds., pp. 1502-1509, Elsevier, Amsterdam, 1988.
 28. Itoh, N., and N. Kasagi, "Turbulence Measurement in a Separated and Reattaching Flow over a Backward-Facing Step with the Three-Dimensional Particle Tracking Velocimeter" (in Japanese), J. Flow Visualization Soc. Jpn., Vol. 9, No. 34, pp. 245-248, 1989.
 29. Kawara, S., "Turbulence Statistics in a Turbulent Separated and Reattaching Flow" (in Japanese), MS Thesis, Dept. Mech. Eng., University of Tokyo, 1990.
 30. Sata, Y., "Study on the Turbulence Near the Solid-Liquid and Gas-Liquid Interfaces" (in Japanese), MS Thesis, Dept. of Mech. Eng., University of Tokyo, 1990.
 31. Gebhart, B., Y. Jaluria, R. Mahajan, and B. Sammakia, Buoyancy-Induced Flows and Transport, Hemisphere, New York, 1988.
 32. Incropera, F.P. and D.P. Dewitt, Introduction to Heat Transfer, 2nd edition, John Wiley and Sons, Toronto, 1990.
 33. Buchhave, P., W.K. George, and J.L. Lumley, "The Measurement of Turbulence with the Laser Doppler Anemometer", Ann. Rev. Fluid Mech., Vol. 11, pp. 443-503, 1979.

APPENDIX A

Preliminary Investigations

A.1 Experimental Data

The following two tables list the combinations of exposure time and flowrate used in the preliminary investigations. Note that the maximum flowrate of the pump, Q_{\max} , is approximately 6.75 L/min, corresponding to an inlet jet velocity of 0.3 m/s.

Table A.1 - Combinations investigated using 100 ASA colour film

TRIAL	EXPOSURE TIME (sec)	f/No.	% Q_{\max}
1	1/8	1.8	54
2	1/15	1.8	54
3	1/30	1.8	54
4	1/8	22	54
5	1/15	22	54
6	1/30	22	54
7	1/8	1.8	93
8	1/15	1.8	93
9	1/30	1.8	93
10	1	1.8	93
11	1/2	1.8	93
12	1/4	1.8	93
13	2	1.8	93

Table A.2 - Combinations investigated using p3200 ASA B&W film
(f/No. = 1.8)

TRIAL	EXPOSURE TIME (sec)	% Q_{\max}
1	2	50,64,90
2	1	50,64,90
3	1/2	50,64,90
4	1/4	50,64,90
5	1/8	50,64,90
6	1/15	50,64,90
7	1/30	50,64,90
8	1/60	50,64,90
9	1/125	50,64,90
10	1/250	50,64,90
11	1/500	50,64,90
12	1/1000	50,64,90

A.2 Calculations

The following procedure was used to calculate the total exposure time. For a given slot i , the exposure time is given by:

$$t_i = l_i / v_d \quad (\text{A.1})$$

where l_i is the circumferential length of slot i in m, given by:

$$l_i = 2\pi R(\theta_i/360^\circ) \quad (\text{A.2})$$

and v_d is the speed of rotation of the disk, in m/s given by:

$$v_i = 2\pi RN \quad (\text{A.3})$$

where R is the radius of the centerline of the slot, θ_i is the angle through which slot i sweeps and N is the number of revolutions of the disk per second. Combining these equations, the exposure time of slot i is given by:

$$t_i = \theta_i / 360^\circ N \quad (\text{A.4})$$

Note that the time of exposure does not depend on the radius of the slot. The total exposure time is comprised of the exposure times of the two slots, t_1 and t_2 , plus the separation time between exposures which is equal to t_2 . With $\theta_1 = 120^\circ$, $\theta_2 = 60^\circ$ and $N = 19.167$ rev/sec (1150 rpm), $t_1 = 1.739 \times 10^{-2}$ seconds and $t_2 = 8.696 \times 10^{-3}$ seconds. Therefore the total exposure time, t_T , is:

$$\begin{aligned} t_T &= t_1 + 2t_2 & (\text{A.5}) \\ &= 1.739 \times 10^{-2} + 2(8.696 \times 10^{-3}) \\ &= 3.478 \times 10^{-2} \text{ seconds} \end{aligned}$$